Precipitate-mediated enhancement of mechanical and electrical properties in HPTE-processed Al–Mg–Si alloy

Vahid Tavakkoli [a,b], Evgeniy Boltynjuk [a], Torsten Scherer [a,c], Andrey Mazilkin [a], Yulia Ivanisenko [a,*], Tamas Ungar [c], Christian Kübel [a,b,d,**]

[a] *Institute of Nanotechnology, Karlsruhe Institute of Technology, Hermann-von-Helmholtz-Platz 1, 76344, Eggenstein-Leopoldshafen, Germany*
[b] *Department of Materials and Earth Sciences, Technical University of Darmstadt (TUD), 64287, Darmstadt, Germany*
[c] *Department of Materials Physics, Eötvös Loránd University Budapest, H-1117 Pázmány P. Sétány 1/A, Hungary*
[d] *Karlsruhe Nano Micro Facility, Karlsruhe Institute of Technology, Hermann-von-Helmholtz-Platz 1, 76344, Eggenstein-Leopoldshafen, Germany*

ARTICLE INFO

ABSTRACT

In this study the effect of high-pressure torsion extrusion (HPTE) and artificial aging (AA) on the strength and electrical conductivity of an Al–Mg–Si alloy was investigated. The resulting material shows remarkable improvement in ultimate strength reaching 380 MPa and in electrical conductivity with 53 % IACS (International Annealed Copper Standard), after post-processing aging at 160 °C for 10 h. X-ray diffraction analysis and electron backscatter diffraction were employed to analyze the structure of the alloy caused HPTE followed by AA. Transmission electron microscopy (TEM) and energy-dispersive X-ray (EDX) spectroscopy were used to study the morphology, elemental composition, and crystal structure of the secondary phases. The study confirms that Guinier-Preston (GP) zones and nano-scale precipitates created during the deformation and subsequent heat treatment are evenly distributed inside the grains. Chemical composition analysis of the precipitates indicated the presence of one main phase based on the Mg/Si ratio coexisting with a low volume fraction of other phases in this Al grade. High-resolution TEM revealed precipitates either with a partially ordered structure or a fully crystalline structure. Strength and electrical conductivity modeling were carried out based on the microstructural characterization results. The findings of this study indicate that HPTE together with thermal treatment has the potential as new approach for processing of commercially significant aluminum alloys.

1. Introduction

The simultaneous achievement of enhanced mechanical strength and electrical conductivity (EC) in materials is of the crucial importance for optimizing electricity transmission efficiency and minimizing service costs for overhead power lines. The usual way to enhance the strength in metals and alloys is strain and solid solution hardening [1]. However, EC is very sensitive to the presence of solute atoms and other structural defects and decreases by any crystal lattice disturbance. This competing nature of EC and mechanical strength attracts high attention in research to establish a way for strength and EC optimization [2,3]. Al–Mg–Si alloys are currently investigated and optimized as conducting materials for overhead power lines due to their high strength-to-density ratio, high EC, satisfactory formability, and low cost [4–6]. For example, Yuan et al.

investigated addition of 0.2 % La to an Al–Mg–Si alloy system and found that La can improve the EC and thermal-resistance properties [7]. However, the mechanical strength slightly decreased by the La addition. Lin et al. [2] enhanced the EC and strength by modifying the thermo-mechanical treatment of an Al–Mg–Si alloy. They showed that pre-aging of samples at 180 °C for 2 h followed by 70 % cold rolling and re-aging at 180 °C for 6 h led to an ultimate strength of 301 MPa and 58.2 % IACS. They pointed out that the simultaneously improved strength and conductivity are mainly attributed to the interaction of strain hardening and precipitation strengthening. Hou et al. [8] proposed high strength - high conductivity Al–Fe wires obtained by cold drawing with a diameter reduction of more than 61.9 %. They believe that the elongated grains, the ⟨111⟩ texture, the low solubility of Fe in Al, as well as the nano-scale precipitates are the four main mechanisms

---

responsible for achieving high strength and high conductivity of the aluminum wire. The influence of natural aging and pre-aging on the strength and EC in drawn a 6201 Al alloy has been investigated by Khangholi et al. [9] They revealed that the combination of natural aging and pre-aging followed by wire drawing and post-aging provided an ultimate strength of 369 MPa with 53 % IACS of electrical conductivity. However, complicated heat treatment along with conventional metal working processes needs vast efforts and time and cannot satisfy the requirements for industrial processing.

Several severe plastic deformation (SPD) techniques have been developed over the last three decades to improve the mechanical strength of materials by producing ultrafine-grained or nanocrystalline materials. Among them, equal channel angular pressing (ECAP) [10], accumulative roll bonding (ARB) [11] and high pressure torsion (HPT) [12] are the most well-known methods, which lead to grain refinement and increased mechanical strength. Valiev et al. [13] introduced HPT to create ultrafine-grained (UFG) structures in Al alloys with enhanced strength and improved EC due to presence of small precipitates. A comprehensive study of HPT-processed 6101 and 6102 Al alloys was performed by Sauvage et al. [14] by means of transmission electron microscopy (TEM) and atom probe tomography. The authors reported that formation of an UFG structure with intra-granular nano-scale precipitates is an effective approach to optimize the combination of strength and electrical conductivity in Al alloys. HPT is one of the most effective methods to synthesize UFG materials by the application of extremely high shear strain. However, the main drawbacks of HPT are the limited size of samples (typically a disk of 10 mm diameter and less than 1 mm thickness), while scaling up requires more powerful equipment, which may be challenging and costly and, hinders its development of industrial applications.

High pressure torsion extrusion (HPTE) [15] has been introduced as a modified version of HPT to provide access to large scale severely deformed materials through a combination of conventional extrusion and high pressure torsion deformation. In HPTE, high shear strain and high hydrostatic pressure are applied to a rod-shaped sample in a single pass. The capability of this method to process rod shape specimens overcomes the main bottleneck of HPT and opens a new window for potential application in industry. Although several studies on sample processing with this method have been done [16–18], none of them investigated its benefits for fabricating of Al conductors for power transmission.

This motivated the study to examine the effect of thermomechanical treatment on structural changes in the 6101 Al–Mg–Si alloy and on its physical properties. The study aims to provide additional insights into the relationship between structural changes (grain refinement, decomposition of a supersaturated solid solution, formation of secondary phases particles) and physical properties (microhardness, yield strength, electrical conductivity), including the influence of individual mechanisms on the physical characteristics of the material. Such a comprehensive study can be a starting point for creating large-size pieces of aluminum alloy that combine both high strength and low electrical resistance, making them appropriate for usage in industry as advanced conductors. In this work, the microstructural evolution under various conditions was investigated using electron backscatter diffraction (EBSD), X-ray diffraction (XRD) and TEM and technique. Subsequently, the influence of individual mechanisms contributing to enhancing electrical conductivity and mechanical strength was studied.

2. Methodology

2.1. Alloy composition and its processing

A 6101 grade Al alloy with a chemical composition Al – 0.94 Mg and 1 Si (at. %) measured by inductive coupled plasma optical emission spectroscopy was investigated in this study. The as-received material for the study was a commercial Al–Mg–Si alloy in a form of rods with a diameter of 12.5 mm, produced by continuous casting and rolling (CSR). Samples for HPTE deformation had a cylindrical shape, 11.8 mm in diameter and 35 mm in length. All samples underwent a solid solution treatment in an air furnace at 500 °C for 1 h and were quenched in water at RT afterwards. The quenched samples were placed in a HPTE die immediately and deformed at 100 °C. The details of HPTE processing are explained in Ref. [15]. The processing was performed with an extrusion velocity (V) of 3 mm/min and a rotational velocity (W) of 1 rpm at a maximum pressure of ~1 GPa. These processing parameters will be denoted as V3W1 thereafter. Molybdenum disulfide (MoS_2) was used as a lubricant to reduce the friction between the die and the sample [19]. Artificial aging (AA) was performed at 130 °C for 48 h and 160 °C for 10 h on HPTE-processed samples.

2.2. Mechanical and electrical properties measurement

Tensile tests were carried out in the extrusion direction of the rod using dog-bone shaped specimens with 10 mm gauge length and 6.85 mm diameter at a constant strain rate of 10^{-3} s^{-1}. The edge part of rod was removed during the sample preparation, so structural investigations were not carried out in it. Three samples were prepared for each treatment condition in order to confirm the reproducibility of the results. Vickers microhardness profiles along the sample diameter in the plane normal to the extrusion direction were measured on a Buehler hardness tester with the load of 50 g and 10 s dwell time. The microhardness value for each point along the measurement line was averaged over at least five measurements. Electrical conductivity was measured on the specimen surface by the eddy current method using a Sigmascope device (Helmut Fischer GmbH) with a frequency of 480 kHz according to DIN EN 2004-1 and ASTM E 1004. Each value was determined as the average of four measurements. Calibration of the device was performed before each measurement with appropriate reference samples.

2.3. Orientation maps

To investigate the microstructural evolution of the specimens processed by HPTE, EBSD mapping was performed using an EDAX Digiview camera mounted on a Zeiss Auriga 60 scanning electron microscope operated at 20 kV. For this, the samples were cut, ground and polished mechanically down to 1 μm using SiC grinding paper. The mechanical preparation was followed by electro-polishing in a QATM - QETCH 1000 setup operated at 10 V and −20 °C with A2 electrolyte from Struers. EBSD patterns were recorded using the EDAX Apex 2.0 software package. The step size for scanning was 0.3 μm. The recorded data sets were indexed using the EDAX orientation imaging microscopy (OIM 8.6) software. The EBSD study was carried out at two different locations (center and middle radius) on both normal and longitudinal sections of the HPTE-processed specimens. The schematic view of the HPTE setup and main external directions related to the sample are shown in Fig. S8. In this work, we consider the misorientation angle range for low angle grain boundaries (LAGBs) to be between 3° and 15°. The lower limit of 3° is chosen to take into account a certain inaccuracy of the measurement, which lies in the range of 1–2° [20].

2.4. XRD measurements

Mechanical polishing and final electropolishing were used to prepare the specimens for XRD analysis. X-ray diffraction measurements were performed using the Empyrean series 3 diffractometer (Malvern Panalytical) with a Cu-Kα anode. XRD measurements were conducted at the center and the middle radius of the samples with a beam diameter of about 1 mm with the step size 0.0167° and in 2θ range 30–120°. The diffraction patterns were evaluated for dislocation density and crystallite size by the Convolutional Multiple Whole Profile (CMWP) procedure [21]. The CMWP method uses experimental XRD profiles to determine the size of coherent scattering domains and dislocation density based on
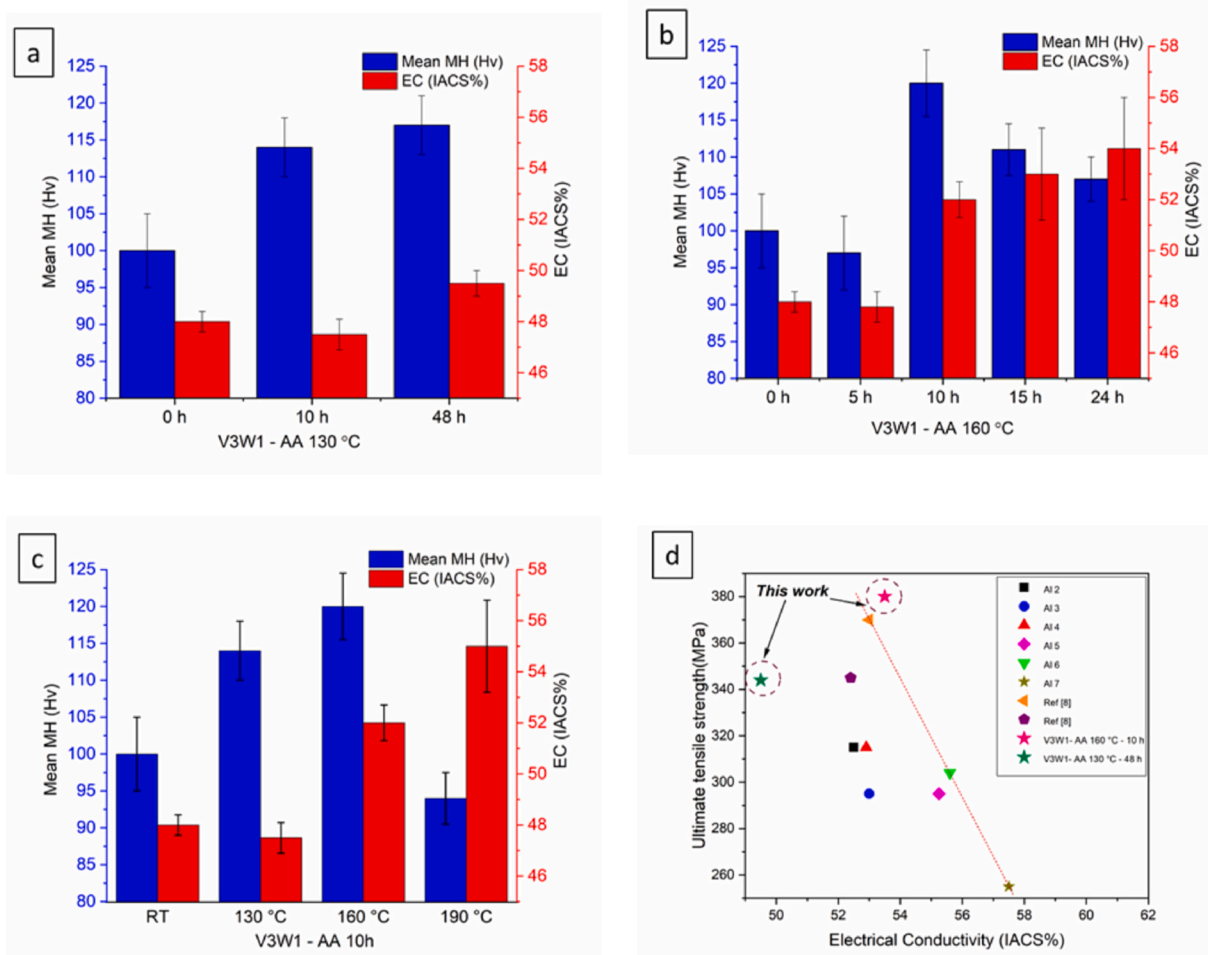
Fig. 1. Averaged HV hardness and EC depending on aging time at (a) 130 °C and (b) 160 °C and depending on (c) aging temperature with 10 h holding time. (d) Comparison of the measured UTS and EC for the alloy studied to the values reported in EN 50183 standard (Al2–Al7) and in Ref. [9].

the physical properties of lattice defects. The calculated profiles are convolved with the instrumental broadening function and compared with the measured patterns using a combination of the statistical Monte Carlo and the analytical Levenberg-Marquardt methods. The instrumental effect was determined by measuring a LaB$_6$ standard specimen under the same diffraction conditions as the investigated samples. The lattice parameters were calculated by using the Fityk software [22]. The uncertainties of the dislocation density were determined based on 3 % confidence interval in Monte Carlo statistical procedure. This number was determined to be 30 %. More details on the procedure can be found in Ref. [21].
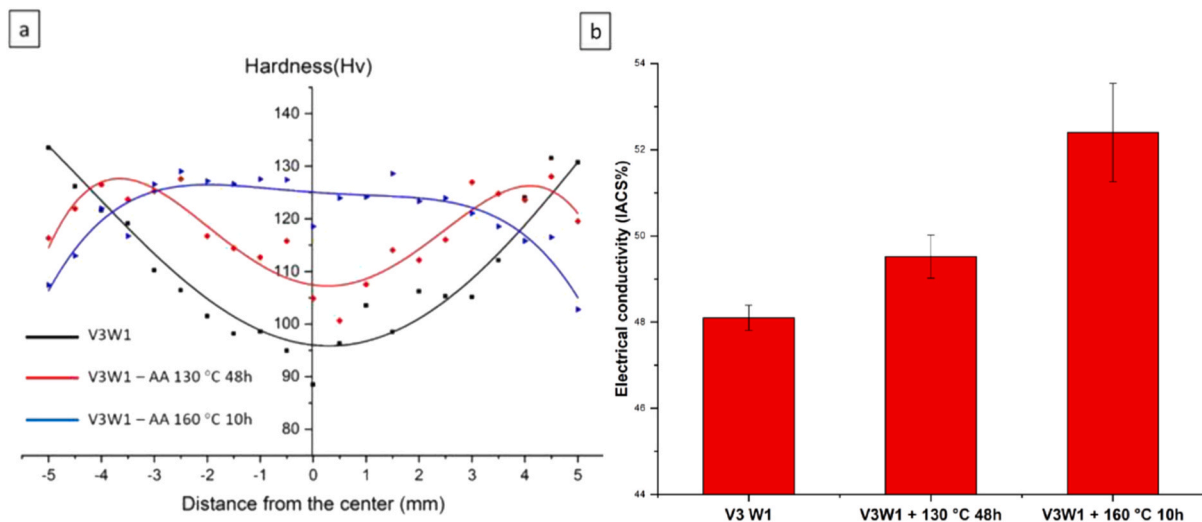

Fig. 2. (a) HV hardness profile along the sample diameter, and (b) EC values for different processing parameters.
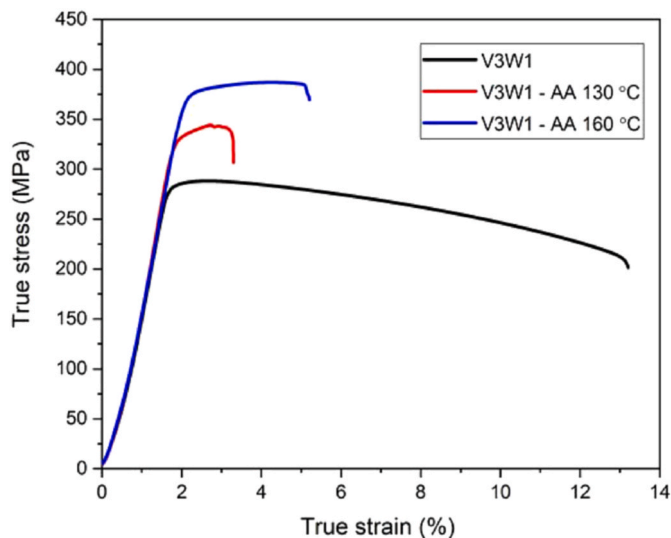
Fig. 3. True stress-true strain curves of the samples in the as-deformed state and after AA at 130 and 160 °C.

2.5. Transmission electron microscopy

Samples for TEM analysis were prepared by a thinning procedure using grinding paper with a roughness down to 150 μm. Afterwards, 3 mm disks were punched out and used for electro-polishing in a Tenupol-5 device (Struers) with Struers A2 electrolyte at 20 V and −20 °C. Conventional and high resolution TEM studies were performed on a double aberration corrected transmission electron microscope Themis Z (Thermofischer Scientific) operated at 300 kV. The foil thickness was measured by electron energy loss spectroscopy (EELS) using a Continuum 963 (Gatan Inc.) spectrometer (Fig. S5). Elemental analysis was performed by energy dispersive X-ray (EDX) spectroscopy using a Super-X detector. JEMS software was used to index the Fast Fourier Transform (FFT).

3. Results

3.1. EC and mechanical properties characterization

We investigated the influence of duration and temperature of AA on microhardness and EC of the HPTE processed samples as shown in Fig. 1. The hardness and EC values reported here are the averaged values measured between the sample center and edge. HPTE deformation and subsequent heat treatment at 130 °C (Fig. 1a) indicates a slight improvement of both hardness and EC after 48 h of aging compared to 10 h aging time. For aging at 160 °C after HPTE deformation, the maximal hardness was reached after 10 h aging (Fig. 1b). The hardness reached a peak value of ~120 HV with EC ~53 IACS%. Fig. 1c compares the HV and EC measured for the samples after the aging for 10 h at 130, 160, and 190 °C. The peak hardness for the sample was found after aging at 160 °C, while EC increased gradually with aging temperature. Fig. 1d shows a comparison of our measured data to values from the EN 50183 Standard for overhead conductor lines [23] and data given in Ref. [9]. It is obvious that the sample prepared by V3W1-AA 160 °C-10 h is beyond the trade-off line between HV and EC. Based on the data obtained, we have chosen the samples aged at 130 °C for 48 h and 160 °C for 10 h for further investigations as they possess an optimal combination of strength and EC.

Fig. 2a shows Vickers hardness profiles along the sample diameter after different treatments. Profile curves are plotted as a result of a nonlinear least squares fit based on the measurement value at each point. The hardness after HPTE deformation is not uniform across the

Table 1

Mechanical properties measured for 6101 grade.

Processing conditions	Yield Stress (MPa)	UTS (MPa)	Uniform Strain (%)	Elongation to failure (%)
V3W1	280	283	2	13.2
V3W1 + AA 130 °C 48h	335	344	2.7	3.3
V3W1 + AA 160 °C 10h	375	381	4.95	5.2

Table 2

Comparison of properties for the 6101 grade (HPTE + AA 160 °C) and for T 81 commercial alloy.

Sample	HV	UTS (MPa)	EC (IACS %)
HPTE + AA 160 °C	125	381	~53
T 81 [14]	90	300	~54

sample. It shows a lower value (~90 HV) in the center compared to edge of sample (~125 HV). This is a well-known phenomenon and comes from the radial dependence of the effective strain distribution and material flow during the deformation as shown in Ref. [24] by finite element method (FEM) simulation. However, surprisingly, for the sample aged at 160 °C for 10 h, the hardness in the center remarkably increased and leveled off. The hardness behavior of this sample is notably different from the others. We suggest that this behavior is due to the difference in phase transformations occurring during aging as all other processing parameters were the same.

Fig. 2b represents the dependence of the electrical conductivity on the processing parameters. It can clearly be seen that electrical conductivity is highly sensitive to the AA temperature. It steadily increases with increasing aging time and temperature and reaches 53 IACS % after the aging at 160 °C for 10 h. Error bars represent the 1σ interval of the statistical distribution of the measurements. The important conclusion from this data is that both the electrical conductivity and mechanical properties improved simultaneously contrary to the typically mutually exclusive trend [2].

The mechanical properties of the as-processed and artificially aged HPTE samples were further characterized by RT tensile test. Fig. 3 displays the true stress-strain curves of the samples. The test results are summarized in Table 1.

The measurements performed show that AA leads to a significant improvement in the strength characteristics of the alloy; the yield stress increases from 260 to 380 MPa. At the same time, the ductility of the alloy demonstrates non-monotonous behavior. The elongation to failure of the sample after AA at 130 °C drops to 3.3 % from 13.2 % in the as-HPTE state, and then improves up to 5.2 % after the aging at 160 °C. However, the uniform elongation was notably improved after AA (Table 1). The uniform elongation of ~5 % observed for the deformed sample after 160 °C heat treatment is higher compared to other two states. The increase in strength is in a good agreement with Vickers hardness behavior and the improved value of the uniform elongation indicates a higher strain hardening capacity. The mechanical properties are compared to the commercially relevant Al alloy temper T81 in Table 2. The substantial improvement in mechanical properties while keeping the EC unchanged, addresses the longstanding challenge of reconciling the mutually exclusive nature of good mechanical and electrical properties. This suggests a possibility to manufacture improved conductors for overhead power lines.

*3.2. Microstructural characterization*

In order to understand the mechanism behind the remarkable combination of EC and mechanical properties, it is necessary to study the microstructure of the alloy in different states.
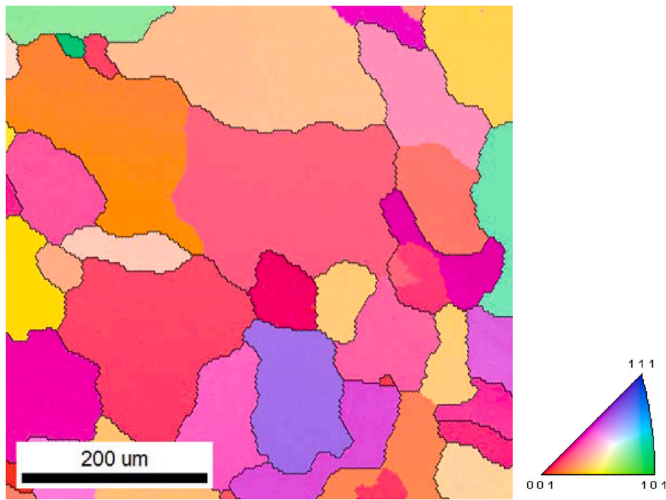
Fig. 4. Orientation map of the sample after the treatment for solid solution. The inset shows the color code for the inverse pole figure map. (For interpretation of the references to color in this figure legend, the reader is referred to the Web version of this article.)

3.2.1. As-deformed state

Crystal orientation maps of the alloy in the initial non-deformed state and after the HPTE deformation acquired in the central part of the sample and the middle radius are shown in Figs. 4 and 5 along with a schematic representation of the studied area location at the processed rod. High angle grain boundaries, HAGB ($\geq 15°$) are traced in the maps in black. The microstructure of the alloy in the initial state mainly consists of the large equiaxed grains with an average grain size of ~100 μm (Fig. 4). The deformation did not lead to a significant grain refinement in the central region of the sample. Fig. 5 shows large grains at the center both in normal and longitudinal direction. It follows from the corresponding misorientation distribution plot, that the microstructure of the sample after HPTE contains a high fraction of LAGBs. In the central part, the fraction of HAGBs is lower in normal view (0.03) than that in longitudinal direction (0.13). The variation in volume fraction can be attributed to the grain morphology, i.e., the coarse grains, containing numerous LAGBs, are elongated in the normal view. The same feature has been reported for HPTE processed copper [18]. However, grain refinement occurred at the middle of the sample radius, which can be seen in both sections (Fig. 6 d, e). The mean grain size was reduced down to ~4 μm in normal view. The fraction of HAGBs increases from the center to the middle radius, which is consistent with the higher strain at HPTE in this sample area. According to FEM, the accumulated strain at HPTE continuously increases from the center of the billet to its edge [24]. The grain structure at mid-radius in normal view appears
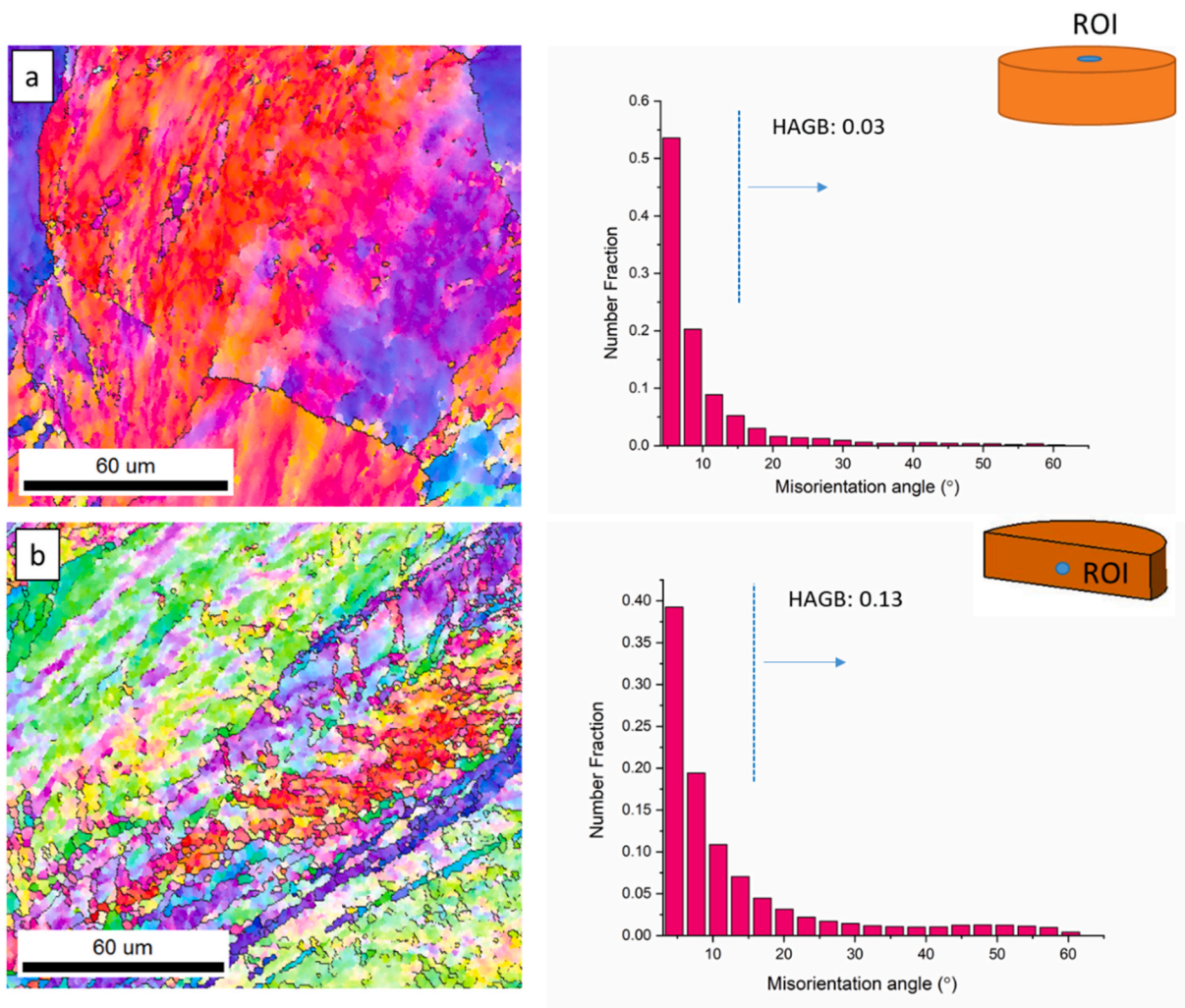
Fig. 5. (left column) Orientation map for (a) normal and (b) longitudinal section at the center of the deformed sample. (right column) Corresponding misorientation distribution plot; the number in the plot shows the HAGB fraction. Inset shows the position of the studied sample in relation to the whole rod.
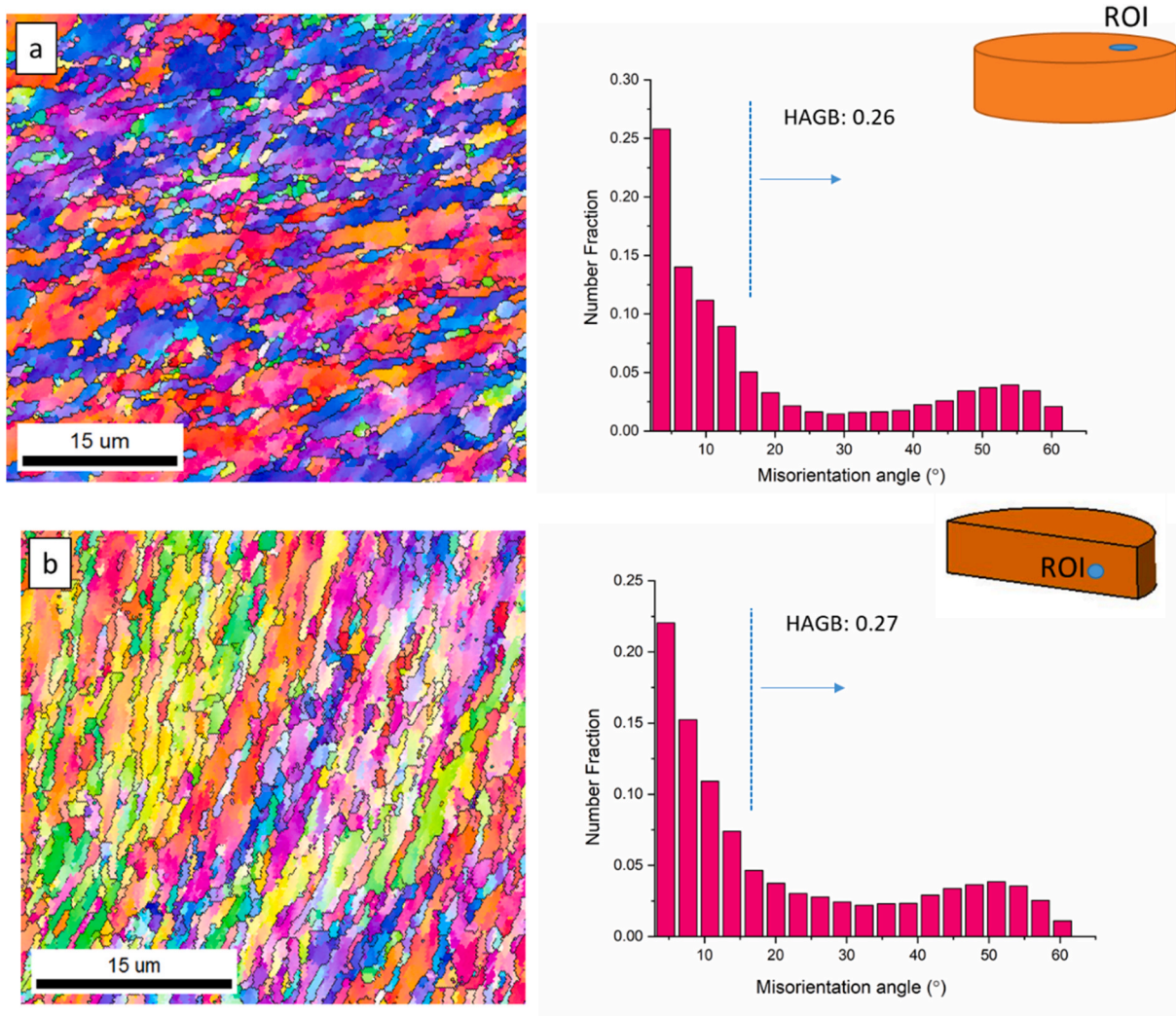
Fig. 6. (left) Orientation map for (a) normal and (b) longitudinal section at the middle radius of the deformed sample. (right column) Corresponding misorientation distribution plot; the number in the plot shows the HAGB fraction. Inset shows the position of the studied sample in relation to the whole rod.

equiaxed, while the severe elongation of the grains with an aspect ratio of ~5 is visible in the longitudinal direction. The fraction of HAGBs in both sections is the same with ~0.26. Such a behavior of the HAGB fraction was also reported in previous studies for copper and pure aluminum after HPTE processing at similar conditions [16,18].

In order to study the microstructure of the alloy in more detail, TEM investigations were performed. A HRTEM micrograph of the HPTE-processed sample at mid-radius is shown in Fig. 7. The location and orientation of the TEM sample in relation to the entire sample rod is depicted schematically as inset in the figure. The image in Fig. 7 was acquired in <001> Al zone axis orientation, which is necessary for HRTEM imaging of typical precipitates in this alloy [25]. In this orientation, precipitates can be observed in cross section and perpendicular to their long axis in the images. The precipitates, which lie in the TEM sample plane exhibit a needle-like shape and are visible due to the strain contrast around them. Dynamic precipitation processes have been observed during the application of different SPD methods in previous studies [26,27], but in the present investigation, the as-deformed sample did not reveal any indication for secondary phase particles. Instead, we only noted the presence of GP zones, which are distinctly visible in the image as denoted by red circle; a higher magnification view of one GP is shown as inset. The corresponding FFT does not show any extra reflections due to the coherency of GP zones with the matrix. The chemical composition of GP zones has not been determined through EDX analysis

in the current study due to their small size.

3.2.2. HPTE deformed + AA at 130 °C for 48 h

Fig. 8 represents the microstructure of the alloy after heat treatment at 130 °C for 48 h. The EBSD orientation map (Fig. 8a) shows that the grain shape and size are similar to those in the deformed sample in agreement with the data reported by Horita et al. for 6101 Al grade, who found that this alloy was thermally stable up to 200 °C [28]. Bright field TEM and HRTEM were employed to reveal the precipitates formed at this temperature, their size and morphology. TEM images clearly show that there are mainly two types of precipitates, which are distributed uniformly in the Al grains (Fig. 8b). HRTEM images presented in Fig. 8c and d illustrate the platelet- and needle-shaped precipitates (shown by red arrows in Fig. 8b). Besides, the presence of GP zones can be inferred based on the pronounced strain contrast observed in Fig. 8b. The majority of the precipitates are arbitrarily oriented in the matrix and their structure cannot be resolved in HRTEM. However, a few of the precipitates reveal several additional reflections in the FFT apart from those of the Al matrix as shown in Fig. 8c (see the inset). However, the corresponding interplanar distances (*d*-values) do not allow unique assignment to one of the phases known for this alloy, like β'', β', U1, U2 or β. Some of the observed phases exhibit rather complex crystal structure with large unit cell sizes. Moreover, the FFT in Fig. 8c contains multiple sets of reflections, which shows that the particle consists of
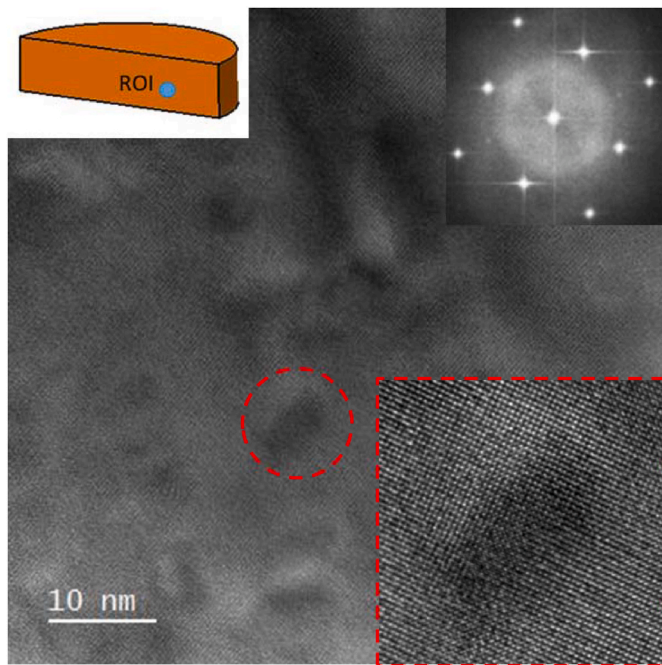
Fig. 7. HRTEM micrograph of the alloy after HPTE deformation; the insets are the schematic location of the TEM sample (top left) and the enlarged view of a GP zone (bottom right).

more than one grain/phase with different orientations. There is no noticeably coherence between precipitates and matrix since none of precipitate reflections in FFT overlap with those of Al.

Nonetheless, another type of well-defined precipitate is also observed (see Fig. 8d). These are coherent needle-shaped precipitates oriented parallel to the <100> crystallographic directions of the Al matrix. Despite the challenges in precise identifying the phases formed in the sample due to their poorly defined structure, it can be argued that these phases are the primary contributors to the hardening of the material.

STEM-EDX elemental maps from a <001> oriented Al grain were collected to obtain data on composition, size, shape and spatial distribution of precipitates. Numerous nano-scale precipitates that nucleated inside the Al matrix are visible in Fig. 9. The precipitated platelets are observed both side-on and edge-on view. Potentially, the phases present in the structure can be identified based on the Mg/Si ratio. However, this value was not evaluated, since the precipitates are very small, and it can lead to a high error in determining their composition.

3.2.3. HPTE deformed + AA at 160 °C

An IPF orientation map is presented in Fig. 10 to show the structural changes that occurred during aging at 160 °C. As mentioned above, the structure of the alloy remains stable up to 200 °C [28], therefore no notable alterations in grain size and shape have been observed for this sample. Nonetheless, the precipitates become larger after the aging at 160 °C (indicated by red arrows in Fig. 10b). A HRTEM image of a selected precipitate is shown in Fig. 10c together with the corresponding FFT. The image does not show a well-defined atomic order, but the FFT reveals the presence of plenty of the crystallographic reflections. Similar to the image in Fig. 8c, they cannot be explained by the typical phases known for this alloy system; rather it is a complex partially disordered structure and may contain different kind of defects. One possible reason for this can be the stored strain associated with defects induced by deformation [29]. Nevertheless, well-ordered precipitates are also present, see e.g., the image in Fig. 10d. The precipitate shows long-range order in the HRTEM image. Analysis of the FFT suggests a structure closely related to the β′ phase with space group P6$_3$/m, a = 0.715, c =
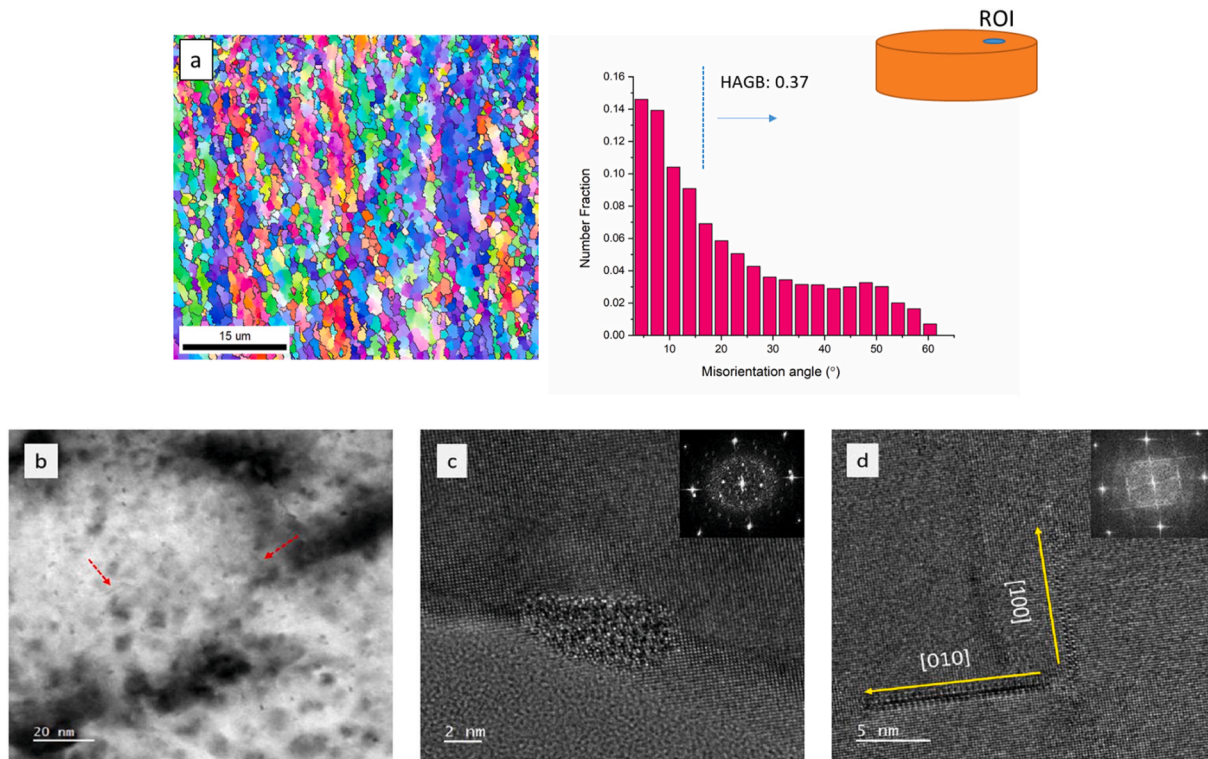

Fig. 8. (a) IPF map of deformed sample + AA 130 °C, and corresponding misorientation distribution plot. Inset shows the schematic illustration of the sample location. (b) bright field TEM and (c, d) HRTEM micrographs at middle radius, normal direction. BF images were collected with the objective aperture inserted to increase the contrast and to reveal the precipitation distribution after aging. The insets in the micrographs are the FFTs showing the <100> orientation of the Al grain.
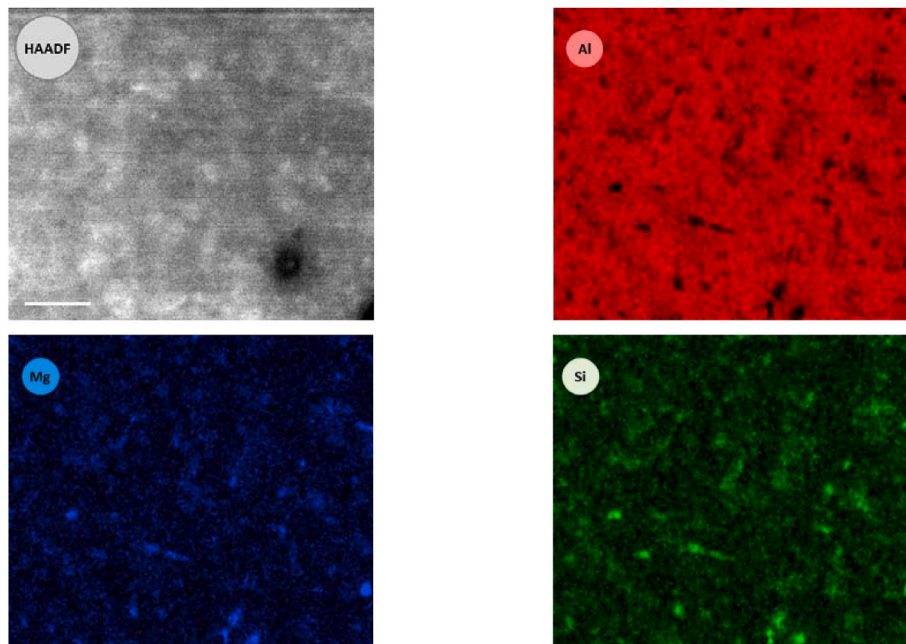
Fig. 9. HAADF-STEM image and EDS elemental maps of Al, Mg, and Si in the deformed sample after aging at 130 °C. The maps were collected for an Al grain in [001] zone axis. The scale bar is 20 nm.

0.405 nm with a small deviation in lattice parameter. For simplicity, it is denoted as β′ phase. However, there is a number of reflections in the FFT which does not belong to the Al or β′ phase. Fourier-filtering of the particle image using these additional reflections reveals that they originate from the peripheral area of the precipitate, as depicted in Fig. S4. Hence, we can describe the structure of the precipitate having a core-shell nature. It also exhibits a well-defined orientation relation (OR) to the matrix $[001]_{Al} \parallel [001]_{β′}$ and $[4\,\bar{1}\,0]_{Al} \parallel [100]_{β′}$. The coherent rod shaped precipitates oriented along the <001> Al directions are also observed in the alloy after AA at 160 °C (Fig. 10e).

Since it was impossible to unambiguously identify the crystal structure of the precipitates using HRTEM, we used the Mg/Si atomic ratio to establish the possible phase composition of the alloy, which we compared with known phases in the Al–Mg–Si system. Although the intermetallic compounds in this system may also contain Al, we could not include the Al ratio in our analysis due to the strong signal from the matrix at the particles, which are much smaller than the thickness of the TEM sample. In order to make a statistically valid conclusion about the composition of the particles, we plotted a histogram of the Mg/Si ratio. This ratio has been determined for a number of particles from multiple EDS elemental maps collected from several TEM samples. In total, we included about 60 particles in our statistics. Fig. 11 shows one of the corresponding EDS elemental maps of a $[001]_{Al}$ grain with precipitates and the corresponding Mg/Si ratio distribution. The graph shows a distribution close to Gaussian and has a significant width, which suggests the coexistence of different phases with a Mg/Si ratio of ~1.2 at its maximum, along with particles demonstrating considerable deviations from this value. This result, along with the TEM data, is additional evidence that the state of the alloy is not at equilibrium.

A visual comparison of the two AA states shows that the size of the precipitates and the average inter-particle distances are different. To assess quantitative characteristics of the alloy after AA at these two different temperatures, we collected the statistics on the size of the precipitates and calculated their number per unit volume (see Table 3). N is the precipitate number density calculated as $N = 3n/A(t+l)$ [30], where n, A, t and l stand for the number of precipitates in the field of view, the area of the field of view, t the TEM sample thickness, and the l is corrected average precipitate length, respectively. The factor 3 is due

to counting only along one of the three <001> Al directions. The thickness was considered to be 30 nm as shown with EELS map in Fig. S6. n is obtained from 4D-STEM dataset (Fig. S5) for the sample aged at 160 °C and dark-field TEM images (Fig. S6) for the sample aged at 130 °C. The precipitate number density increased from $(1.5 \pm 0.3) \times 10^{23}$ m^{-3} at 130 °C to $(2.2 \pm 0.5) \times 10^{23}$ m^{-3} at 160 °C.

The precipitate diameter distributions were plotted for approximately 200 particles based on several dark-field TEM images (Fig. S6). The plot for the sample after AA at 130 °C (Fig. 12a) shows a particle size distribution with an average diameter of ~1.4 nm, whereas the sample aged at 160 °C exhibits a bimodal distribution (Fig. 12b). The majority of particles with a smaller size contribute to a Gaussian distribution with a maximum at ~2.2 nm. Larger particles have an average size of ~5 nm. Thus, the increase in annealing temperature leads to a growth of the precipitates. However, the fraction of the bigger particles is small (~7 %).

3.2.4. Precipitate free zone and grain boundary precipitates

Precipitate free zones (PFZ) were observed near grain boundaries after AA as shown in Fig. 13. Generally, PFZs are a typical phenomenon in dispersion hardened alloys after AA [31–33]. The mechanism of the PFZs formation is diffusion of solute atoms towards grain boundaries. This creates a zone depleted of vacancies and solute elements, which hinders the formation of precipitates. The width of this zone depends on the activation energy for diffusion and the nature of GBs as was studied in details in Ref. [34]. Our measurements showed the formation of particles at the GBs with a size of approx. 20 nm and a PFZ width of ~30 nm after aging at 130 °C. Aging at a higher temperature (160 °C) leads to an increased size of the GB precipitates up to 50 nm and a corresponding PFZ width of about 80 nm. We also plotted the Mg/Si distribution for the particles that precipitated along the grain boundaries (Fig. 13b). This distribution is much narrower than that for precipitates formed inside the grains. The composition maximum is at a higher value of Mg/Si ~1.6 compared to the intra-granular precipitates. Thus, the phase observed at the grain boundaries after AA at 160 °C differs from the dominant phase inside the grains.
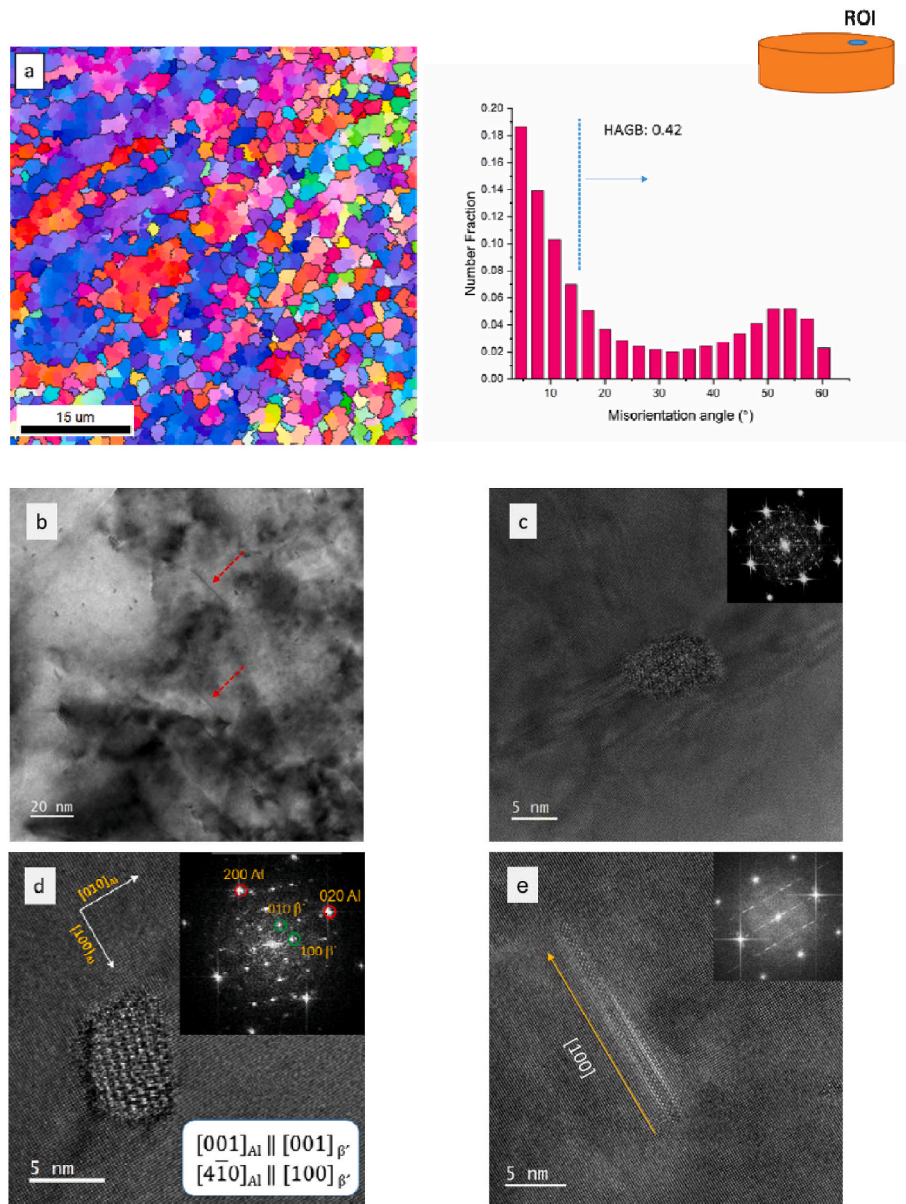
Fig. 10. (a) IPF orientation map of the deformed sample + AA 160 °C, and corresponding grain boundaries misorientation distribution plot. The inset shows the schematic illustration of the sample location. (b) Bright field TEM and (c–e) HRTEM micrographs. BF images were collected with the objective aperture inserted to increase the contrast and to reveal the precipitation distribution after aging. The insets in the micrographs are the FFTs showing the <100> orientation of the Al grain together with the reflections of the precipitates. In (d) the reflections are denoted by red circles for Al and by green circles for the β' phase. The inset is OR of the precipitate to the matrix. (For interpretation of the references to color in this figure legend, the reader is referred to the Web version of this article.)

3.3. X-ray diffraction analysis

As mentioned above, the EBSD study revealed a gradient in grain size along the sample radius which is explained by the inhomogeneous strain distribution at HPTE [15]. Analysis of the XRD profiles has been used to determine the lattice parameter of the Al-based solid solution (a) and to estimate the dislocation density (Λ) in different parts of the sample [21]. Fig. 14 presents the XRD patterns of the deformed and aged samples collected at the center and the middle radius. Note that only Al reflections are present and no peaks for the precipitates are detected due to their low volume fraction and small size. The results of the XRD profiles analysis are summarized in Table 4. Taking into account the step size value, pattern range and the signal to-noise-ratio, the relative measurement uncertainty of the lattice parameter is estimated to be $\sim 4 \times 10^{-4}$ Å [35]. The details of the error estimation can be found in the SI. The results of the XRD patterns evaluation by means of CMWP are

shown in Fig. S2. According to the data obtained, no noticeable dependency of dislocation density on the distance from the sample center is revealed. The value is about 6×10^{14} m^{-2} at the mid-radius and 8×10^{14} m^{-2} in the center of the sample. The dislocation density decreased slightly to $(3 \div 5) \times 10^{14}$ m^{-2} after AA due to thermal recovery, but its magnitude remains at a rather high level (see Table 4). We also measured the dislocation density by means of the interception method using the HAADF STEM images of the deformed sample + AA 130 °C. This gave us a similar value of around 6.6×10^{14} m^{-2} for the mid-radius region (Fig. S3).

The measured lattice parameter of the quenched sample is ~ 4.0574 Å. The a value after HPTE deformation is marginally decreased (see Table 4). A significant decrease in the Al lattice parameter was found for the samples after AA. The lattice parameter after deformation in the center of the sample is ~ 4.0571 Å and after aging at 130 and 160 °C, it decreases to ~ 4.0561 Å and 4.0541 Å. The decrease of the lattice
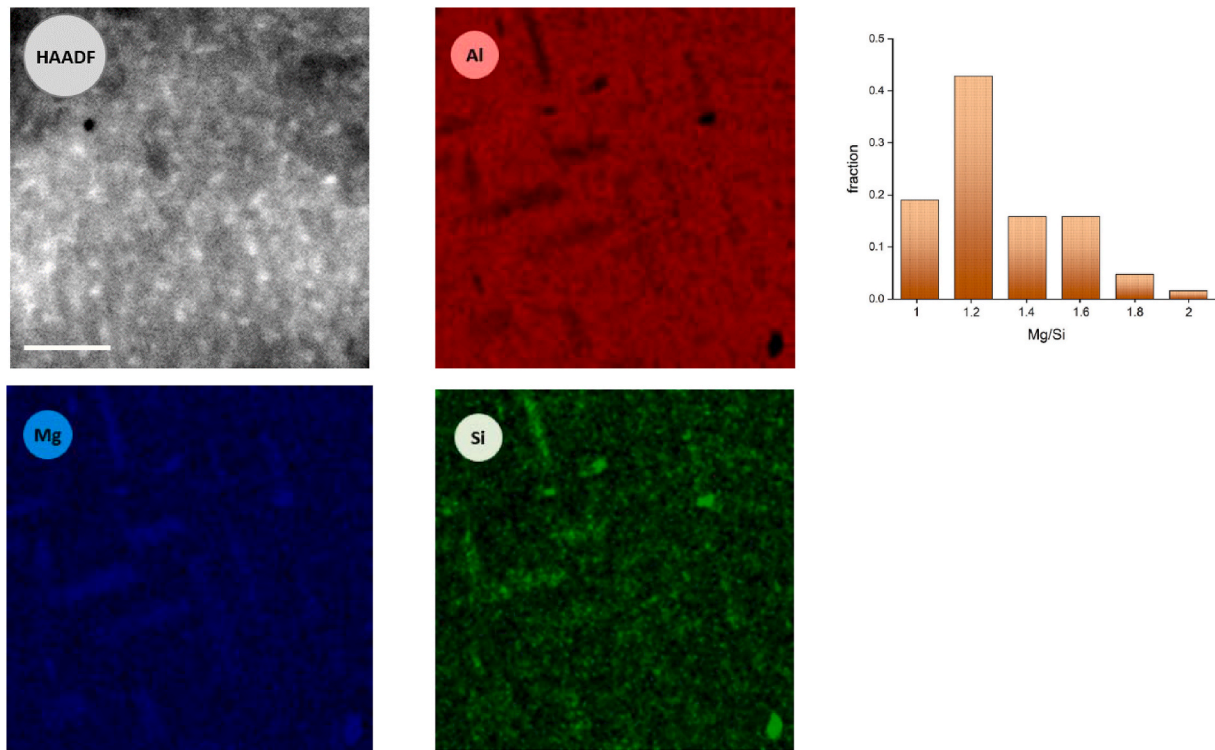
Fig. 11. HAADF-STEM image and EDS elemental maps for Al, Mg, and Si of the deformed sample after aging at 160 °C. The maps were collected for Al grains in [001] zone axis orientation. The scale bar is 50 nm. Distribution of the Mg/Si ratio of the intra-granular precipitates.

Table 3
Parameters of the alloy structure based on TEM-DF and 4D-STEM measurements.

Processing conditions	Averaged particle diameter, nm	Precipitate density, m^{-3}
V3W1 + AA 130 °C 48h	1.4	1.5×10^{23}
V3W1 + AA 160 °C 10h	2.2	2.2×10^{23}

parameter is associated with the segregation from the solid solution.

4. Discussion

The strength and electrical conductivity of an alloy is closely related to the microstructural characteristics. Below we discuss in detail the mechanical properties, evolution of the microstructure of the A6101 alloy and the individual contributions responsible for changes in strength and electrical conductivity considering their relationship with the observed structural differences.

4.1. Mechanical properties

As can be seen from our measurements (see Fig. 2a), the hardness profile along the diameter for samples in the as-deformed state and after AA at 130°C shows a V-shape, typical for materials after treatment by means of HPT. From this point of view, the hardness behavior of the AA160-10h sample is not quite usual; the sample demonstrates an almost constant hardness value along the radius from the center to its edge. In general, hardness is predominantly influenced by two key parameters: 1) the density of defects, such as grain boundaries and
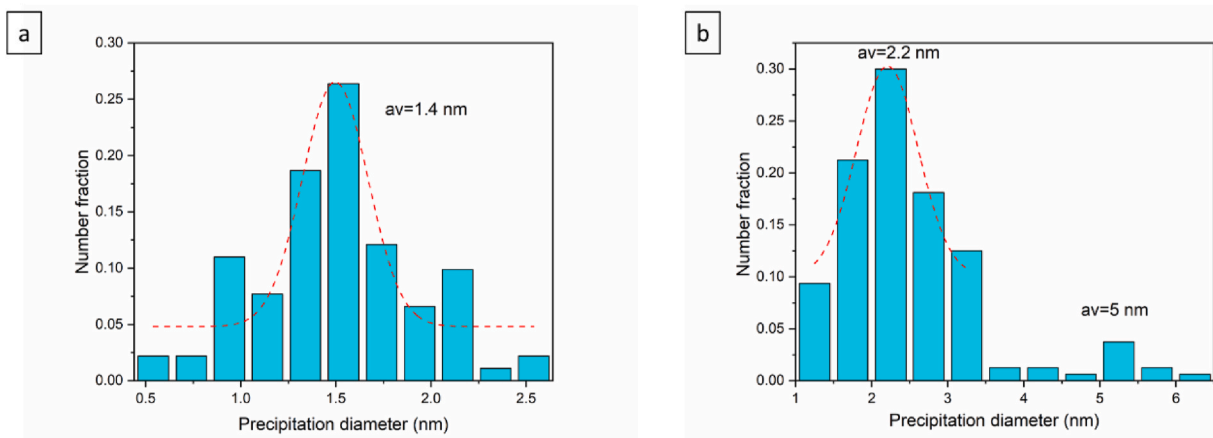
Fig. 12. Precipitates diameter distribution for the samples after AA at (a) 130 °C and (b) 160 °C.
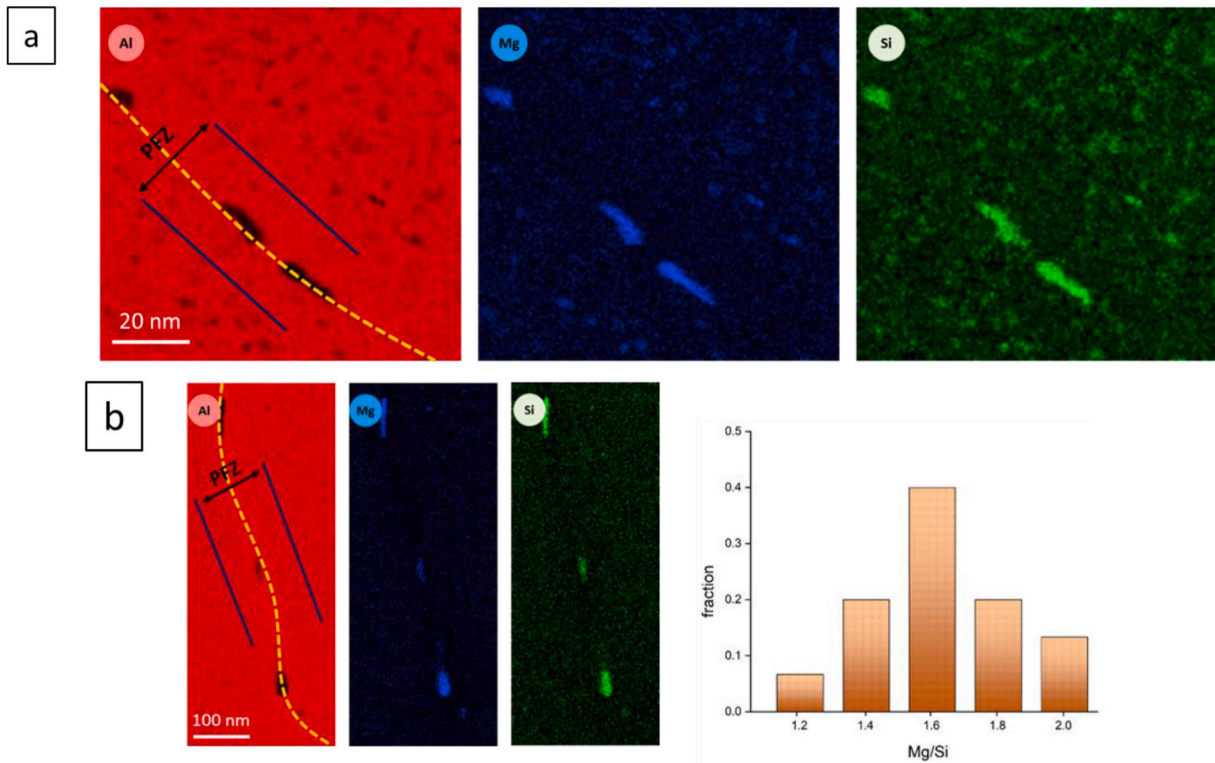
Fig. 13. EDS elemental maps for Al, Mg, and Si of deformed sample after AA at (a) 130 °C and (b) 160 °C demonstrating the formation of PFZ and Mg/Si distribution plot for the particles precipitated at grain boundaries.
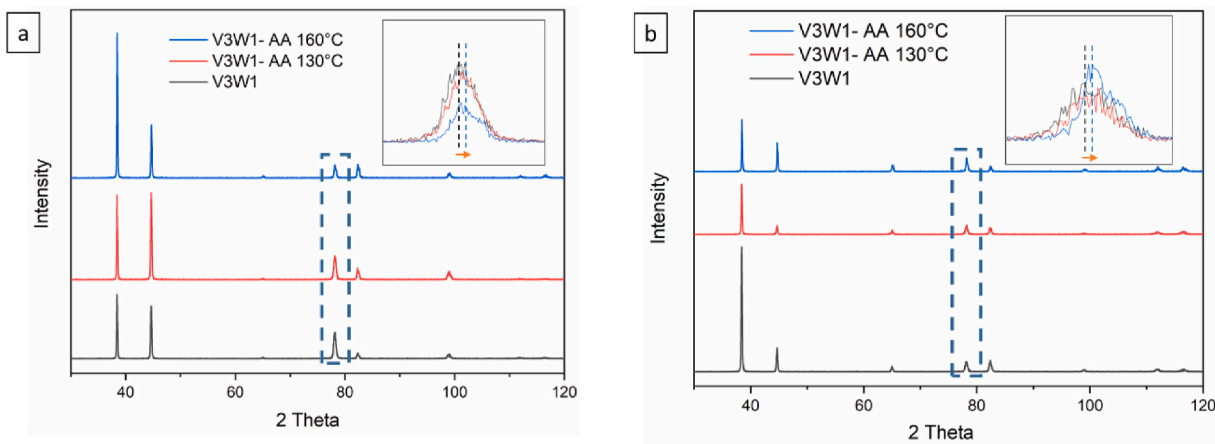

Fig. 14. XRD diffraction patterns of the HPTE-processed sample followed by AA collected at its (a) central and (b) mid radius part. The inset shows enlarged (311) peak.

Table 4
Dislocation density and lattice parameters evaluated from the XRD profiles using the CMWP method.

Sample	Dislocation density (m^{-2})		Lattice parameter (Å)	
	Center	Mid-radius	Center	Mid-radius
Quenched	$\sim10^{10}$–10^{11} [30]		4.0574	
V3W1	8×10^{14}	6×10^{14}	4.0571	4.0569
V3W1- AA 130 °C	4×10^{14}	3×10^{14}	4.0561	4.0561
V3W1- AA 160 °C	5×10^{14}	4×10^{14}	4.0541	4.0518
Accuracy: ±30 %			Accuracy: ±0.0004 Å	

dislocations, generated during deformation, and 2) the size and volume fraction of precipitates formed during AA. Since the grain size (see EBSD maps in Figs. 6, 8 and 10) and dislocation density (see Table 4) for the samples in as-deformed state and in the state after AA at 160 °C are close, precipitates play the main role in the hardness leveling-off behavior. We did not conduct detailed studies of the precipitates characteristics in the central part of the samples. A meaningful statistically reliable analysis is limited by the fact that the aluminum grains in the central region of the samples are very large. Therefore, further extensive research beyond the scope of this article is necessary to comprehensively consider this aspect.

Additionally, the formation of precipitates at grain boundaries can create PFZs along the boundary line, leading to some degree of softening in the sample. Typically, the grain boundary precipitates have less effect
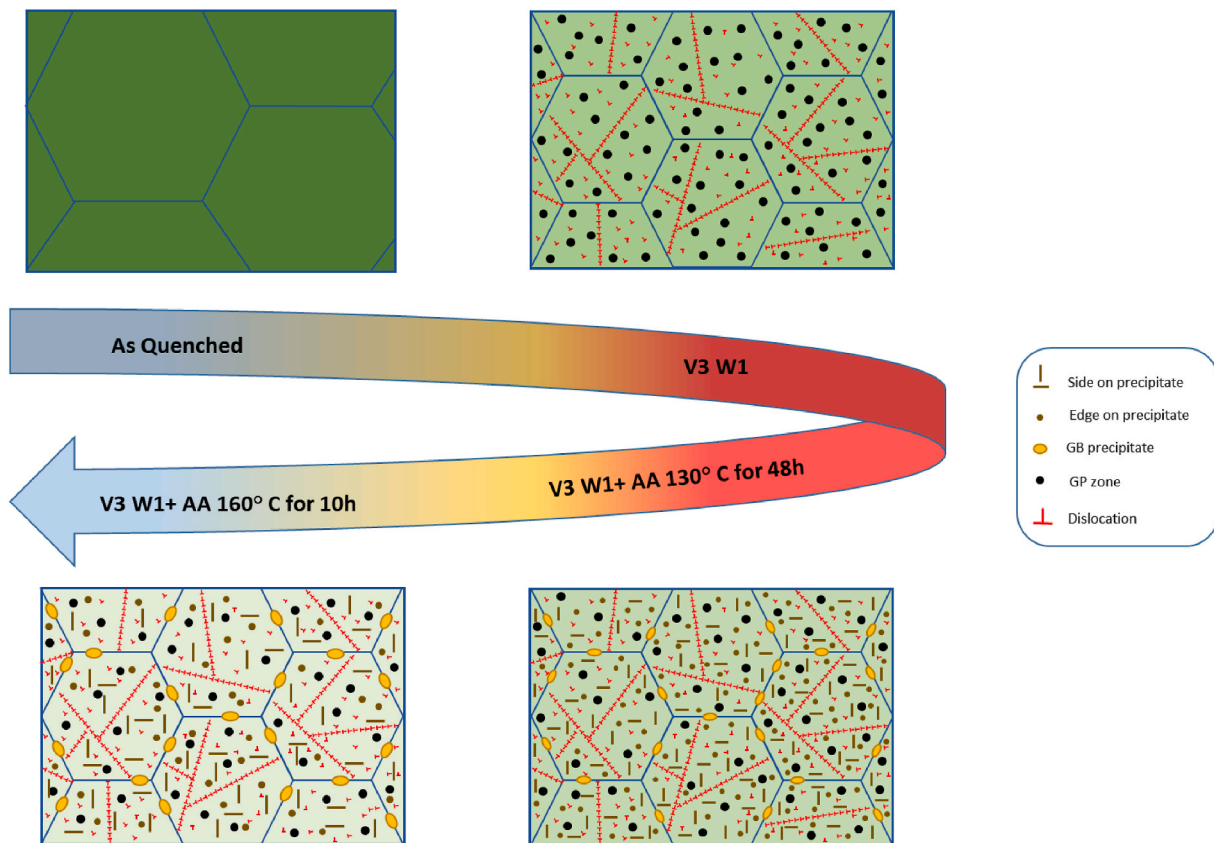
Fig. 15. Schematic illustration of microstructure evolution of 6101 Al grade after quenching and during the HPTE followed by AA in the mid-radius region of the sample. HPTE induces a high dislocation density resulting in grain refinement and the formation of dislocation walls; GP zones are observed in Al grains. Annealing at 130 °C leads to the precipitation of particles and development of PFZs. Raising the annealing temperature to 160 °C causes an increase in size of both the precipitates and the PFZs. The background color indicates the concentration of solutes in the matrix. (For interpretation of the references to color in this figure legend, the reader is referred to the Web version of this article.)

on the hardening behavior compared to intra-granular particles due to less coherence. With larger grain size in the sample center, a larger fraction of precipitates forms inside the grains, thereby contributing more significantly to hardening. The influence of these precipitates can be seen also in tensile test. From the data in Tables 1 and it is clear that the samples after AA demonstrate higher strength characteristics and lower uniform elongation compared to the deformed sample. The presence of intermetallic phase particles in the structure leads to an increase in the strength of the material while simultaneously reducing ductility [36,37]. The effect of precipitates on plasticity may depend on a number of factors, such as their size, lattice alignment to the matrix material, the number density of these precipitates, and the uniformity of their distribution in the volume of the sample. The studies we carried out confirmed the strengthening effect of the secondary phase formed after AA. From the data in Tables 1 and 3, the strength of the V3W1-AA130°C48h sample is lower than that of V3W1-AA160°C10h due to the lower precipitates number density and their smaller size. An additional decrease in ductility in aged samples is also associated with the formation of a PFZ along the grain boundaries. This leads to the appearance of structural inhomogeneity and contributes to premature fracture [38].

A potential explanation for the increased ductility observed in V3W1-AA160°C10h compared to V3W1-AA130°C48h may lie in the size of the precipitates and their coherence with the aluminum lattice. Peng et al. reported through large-scale molecular dynamic simulations that densely dispersed nano precipitates can simultaneously act as dislocation sources and obstacles, providing a balance between deformability and local hardenability to achieve enhanced ductility [39]. Therefore, it is plausible to suggest that the size and spacing of precipitates in sample

V3W1-AA160°C10h may interact more favorably to achieve an optimal balance between strength and ductility.

4.2. Microstructure and precipitate evolution

Based on the TEM and EBSD results, we can summarize the microstructural evolution of A6101 Al at the mid-radius of the sample during the HPTE deformation followed by AA at different temperatures as shown schematically in Fig. 15.

Severe plastic deformation of the aluminum alloy leads to a significant increase in the dislocation density in the material, however the structure is not uniform across the deformed rod as can be (see results of EBSD and XRD measurements). Dislocations are organized in subgrain boundaries (dislocation walls); the share of LAGB is high and comprises ~ 75–90 % depending on the location in the sample. In the as-deformed state, no presence of secondary phase particles was detected, but the formation of GP zones was observed (see Fig. 7b). It is practically impossible to quantify the volume fraction of GP zones from TEM images, since they are very small and coherent with the matrix.

The aging of the as-deformed sample did not lead to a noticeable grain growth or a significant decrease in the dislocation density. It was expected that the dislocation density would decrease rapidly during aging due to the high stacking fault energy of Al. However, the presence of precipitates significantly impedes the motion of dislocations due to the localized stress fields around the particle. As a result, the motion of dislocations is blocked, which prevents their effective annihilation during annealing and a significant dislocation density is retained in the structure.

The aging process leads to a transformation of GP zones into

secondary phase particles. During aging at 130 °C, intra-granular precipitates with an average diameter of ~1.4 nm formed. Observing the enhanced mechanical strength as depicted in Fig. 5, we can infer that this improvement is attributed to the semi-coherent characteristics of the precipitates. They can block dislocation glide effectively, and dislocations are the dominant plasticity carriers in crystalline solids [40]. Subsequent aging at a higher temperature (160 °C) led to an increased size of intra-granular precipitates with a distribution of the Mg/Si ratio implying the presence of one main phase and other phases of different composition coexisting (Fig. 11). The increased precipitate size and density in this state plays a decisive role in a more effective pinning of dislocations, as evidenced by the high strain hardening capacity of the material, demonstrated in tensile tests (Fig. 4).

For Al–Mg–Si alloys after solid solution treatment, the common sequence of phase formation with increasing temperature and aging time has already been established [41]. First, the solute atoms cluster, which leads to the formation of GP zones. Then a metastable β''-phase is formed. This is followed by the formation of β', U1, U2 and β phases. The β''-phase is reported to be the most important hardening phase in the Al–Mg–Si system, but its formation can be suppressed by accumulated strain [42,43]. In this case, β' dominates dispersion strengthening. The β-phase, as the last one in this series, is not coherent with the Al matrix and does not contribute significantly to the strengthening of the material [44,45]. Recent HRSTEM and *ab-initio* studies have shown that the most likely chemical composition of the β''-phase is either $Mg_4Al_3Si_4$ or $Mg_5Al_2Si_4$, which is energetically more favorable [46]. The results of our EDX measurements do not allow us to conclude if aluminum is present in the precipitates, but the measured Mg/Si ratio (Fig. 11) is approximately 1.2, which remarkably fits the latter of the two compounds. We determined the crystal structure for one of the particles using HRTEM, which corresponds to the β' phase with the composition $Mg_6Si_{3.3}$ and Mg/Si ~ 1.8 (Fig. 10d). However, it should be noted that a single HRTEM image may not be representative and the crystal structure of most of the particles was not determined due to the lack of the well-defined atomic order.

Nucleation and growth of particles can occur either due to accelerated bulk diffusion of solute atoms or due to their enhanced diffusion along dislocations. The dislocations present in the structure provide energetically favorable sites for the nucleation and growth of the precipitates [47]. It is known that the presence of dislocations increases the diffusion rate by almost three orders of magnitude compared to that in the bulk of the material [48].

During aging of the deformed alloy, there is no sequential process for precipitation of hardening phases, but they coexist at the heat treatment conditions. The highly defective, non-equilibrium structure of the formed precipitates is apparently due to the deformation applied during HPTE [42] and results in the accelerated growth of the particles due to enhanced diffusivity of the solutes. At the same time, some particles after aging at 160 °C exhibit a well-defined structure (see, for example, Fig. 10d).

The precipitation of the secondary phase particles is associated with the decomposition of the supersaturated Al-based solid solution. This process can be monitored by changes of the Al lattice parameter. In the deformed sample, as well as in the sample after subsequent AA, the lattice parameter is smaller in the mid-radius region compared to the center. As the AA temperature increases, the lattice parameter continues to decrease. Thus, based on the XRD analysis, we can conclude that the content of solute atoms in the solid solution decreases and this effect is more pronounced at the mid-radius compared to the center of the sample. This is explained by the higher applied strain, and, consequently, an increased concentration of defects, which contribute to an increase in the diffusion mobility of solutes.

Accelerated grain boundary diffusion gives rise to the formation of phases with higher Mg/Si ratio and PFZs along the grain boundaries (see Fig. 13). The width of PFZs increases with increasing aging temperature. A comprehensive investigation of the PFZs was not the aim of the present study, but PFZs were found for both states of the alloy after AA. The presence of PFZs in the aged alloys can be essential for the mechanical characteristics of the material, since they are a limiting factor for the ductility. Previous studies have shown that PFZs are softer close to grain boundaries and upon deformation tend to localize stress and cause premature failure [49]. The study in Ref. [50] showed that the width of the PFZ is an important parameter; a narrow PFZ can promote strain localization, which leads to faster nucleation of voids and growth of particles at grain boundaries.

In addition, the presence of nano-sized precipitates within the grain can have a detrimental effect on ductility by promoting the development of dislocation pile-ups in their vicinity. Consequently, this phenomenon leads to stress concentration and microcracks [39]. However, the same precipitates play a crucial role in enhancing the accumulation of dislocations within the material. As a result, they significantly improve the strain hardening capacity of the material. This effect is evidenced by the enhanced uniform elongation in the HPTE processed sample after aging at 160 °C, which reveals a remarkable capacity for dislocation storage in this particular state.

It is worth noting that, given the grain size, grain boundary precipitates only slightly affect hardness and electrical conductivity, while intra-granular precipitates are the main strengthening factor [51]. In general, it can be said that despite the presence of PFZ, the obtained samples exhibit a high level of plasticity.

Thus, we can conclude that after AA at 160 °C, the material demonstrates the highest EC value along with a reasonable ductility (Figs. 3 and 4). This result is achieved in total due to the formation of intra-granular precipitates and the effect of solid solution purification. It can be clearly stated that the ability of HPTE to subject specimens to different strain makes it possible to tailor defect densities to tune mechanical strength and EC.

4.3. On the origin of strength and EC improvement after AA

The application of Al–Mg–Si alloys as overhead conductors requires a combination of both high strength and high EC. Grain boundaries, dislocations, precipitates and solutes lead to strengthening of the material, but impair EC. Therefore, the trade-off between electrical and mechanical properties is a bottleneck in the tailoring the alloy properties. In this study, we demonstrated that these two characteristics can be increased simultaneously within a certain range of AA temperatures, as shown in Fig. 2. The measurements of the properties after HPTE and subsequent aging at 130 and 160 °C showed improved mechanical and electrical properties in both cases (Fig. 3). The best results were obtained for the deformed sample after AA at 160 °C, which demonstrates a noticeably increased EC while maintaining a high level of microhardness and tensile strength. This behavior is associated with the formation of secondary phase particles inside the Al matrix, as shown by TEM study (see Figs. 9 and 10). After AA at 160 °C, the precipitates are larger in size and more densely packed than after AA at 130 °C. Changing the particle size has two mutually exclusive effects on the strength of the sample. Larger particles, either coherent or semi-coherent, are more effective at impeding dislocation glide because dislocations require more force to overcome the obstacle; accordingly, the material has greater strength. The mechanism by which dislocations overcome a particle, i.e., passing through it or bending around it and form an Orowan dislocation loop, depends on its and the degree of coherence with the matrix. On the contrary, a sparser distribution of particles results in reduced number of blocking points and, accordingly, a decrease in strength. Since the overall strength of the material increases, we can conclude that the first of these two processes predominates.

With regard to EC, it is well known that it is directly proportional to mean free path of conducting electrons. All factors disturbing the free electron path will increase the resistivity. The mechanism behind it is scattering of free electrons by thermal lattice vibrations and by lattice defects such as grain boundaries, dislocations and solute atoms.
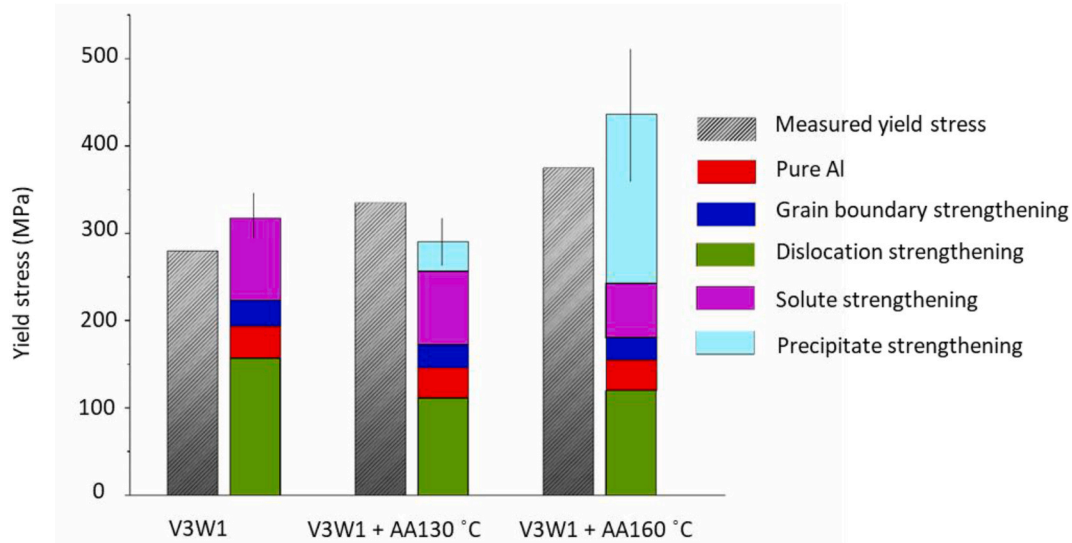
Fig. 16. Comparison of the measured strength and the modeled values for the as-deformed sample and after AA at 130 and 160 °C based on the measured structural characteristics. Different colors show the contributions from different mechanisms. (For interpretation of the references to color in this figure legend, the reader is referred to the Web version of this article.)

Formation of GP zones in the deformed samples reduces the EC, since they scatter electrons strongly due to lattice distortions. The improved EC after AA stems from purification of the matrix from dissolved atoms and removing coherent clusters (GP zones) by transformation to semi- or incoherent particles. TEM results indicate that the rapid increase in conductivity correlates with the precipitation of hardening phases [52]. With increased aging temperature, the phases grow by consuming the dissolved atoms from the matrix [48], which results in the increased EC. Although the precipitates can hinder the movement of conducting electrons and potentially degrade the EC, their impact is relatively minor compared to solutes. The reduced concentration of solute atoms significantly enhances the likelihood of electrons passing through the matrix without scattering. As discussed above, dislocations enhance the diffusivity of solutes atoms and cause a more rapid depletion of Mg and Si solute content in the matrix, ultimately resulting in increased EC. This result is confirmed by XRD measurement (Fig. 14). The decrease in solute concentration in the Al-based solid solution is associated with the formation of secondary phases that consume alloying elements (Mg and Si), which leads to a decrease in the lattice parameter. A similar correlation between the change in the lattice parameter and the magnitude of the electrical conductivity has already been reported in previous studies [53,54].

4.4. Strength modeling based on microstructural parameters

Strength and EC can be modeled based on microstructural features. The model for the deformed sample aged at 160 °C is presented here as it shows the best tradeoff relationship between strength and EC. The modeling parameters for other states can be found in SI and the modeling results are shown in Fig. 16. Several strengthening mechanisms are known for the metallic materials. These are precipitation or age hardening, solid-solution strengthening, dislocation or work hardening, and grain-boundary (Hall-Petch) hardening. By modeling the mechanical strength with different hardening mechanisms, it is possible to estimate the yield strength of an alloy in a given state, assuming that the contribution of each mechanism is additive:

$$\sigma_{total} = \sigma_{f\ Al} + \sigma_{dis} + \sigma_{prec} + \sigma_{GB} + \sum \sigma_i^{SS} \tag{1}$$

Here, $\sigma_{f\ Al}$ is the friction strength of pure Al and σ_{dis}, σ_{prec}, σ_{GB}, σ_i^{SS} represent dislocation hardening, precipitation hardening, Hall-Petch effect, and solid-solution strengthening. The yield stress of the

aluminum matrix is around 35 MPa according to the data for annealed pure 1100-O aluminum [55].

The Bailey-Hirsch relationship can be applied to estimate the contribution of dislocations to the strength [56]:

$$\sigma_{dis} = \alpha MGb\Lambda^{1/2} \tag{2}$$

where $\alpha = 0.3$ is a dimensionless constant for Al, $G = 26.9$ GPa is the shear modulus of Al, and $b = 0.29$ nm is the Burgers vector of ½<110> full dislocations in the Al lattice [57]. M is the Taylor factor, which was determined from EBSD datasets. The Taylor factors for different alloy states are shown in Table S3. The dislocation density Λ for the deformed sample after AA at 160 °C was estimated to be ~4×10^{14} m^{-2} by means of X-ray line profile analysis (see Table 4) with an accuracy ~ 30 % [21]. Therefore, the contribution of dislocations to the yield strength is ca. 120 ± 20 MPa.

The well-known Hall–Petch equation can be used to estimate contribution from grain boundaries to the strength [58]:

$$\sigma_{GB} = k_{HP}d^{-1/2}, \tag{3}$$

where k_{HP} is a Hall-Petch constant taken as 0.06 MPa·m$^{1/2}$ [59] and d is the average grain size. The grain size at mid-radius differs in normal and longitudinal section of the sample. However, average value of 6 μm was considered, which led to $\Delta\sigma_{GB} = 24 \pm 6$ MPa.

The strength contribution from the secondary phase precipitates σ_{prec} is caused by either shearing or bypassing of the particles by dislocations, depending on their size. According to the methodology described in Refs. [9,14,30], the increase in yield strength is related to the average strength of an obstacle F. They considered all precipitates to be non-shearable, however there was not enough justification provided for this assumption.

In our study, the particle size distribution exhibits a bimodal character (Fig. 12b). First, we considered the part with a smaller size as shearable, and that with a larger size as non-shearable. To calculate their contributions to the strength the corresponding formulas were used:

For shearable particles [30].

$$\sigma_{prec}^{shear} = \frac{M}{b^2\sqrt{\beta G}}\sqrt{N \cdot r} \cdot F^{3/2}. \tag{5}$$

with G and b being defined as above, β is a constant ($\beta = 0.28$), r is the precipitate radius. N is the number of particles and the obstacle strength

for shearable precipitates is determined to be $F = 2\beta Gb^2(r/r_c)$ with r_c being the transition radius between particle shearing and bypassing. This term is usually considered to be 2.5 nm [30].

For non-shearable particle the Orowan mechanism is active and the corresponding strength can be calculated using $\sigma_{prec}^{Orowan} = \frac{2M\beta Gb}{L}$, where M, β, G and b were defined above. L is inter-particle spacing, which was calculated as $L = N^{-1/3}$ [9].

It is important to mention that the contribution of the precipitate hardening to the yield stress is decisive. It directly depends on the particle number density; therefore, counting accuracy is critical. Accurate determination of the particle density is challenging due to factors like sample thickness variation, non-uniform distribution, and low precipitates image contrast, leading to notable counting errors. Only a fraction of the precipitates is visible in dark-field images, *viz.* those whose diffraction beams pass through the objective aperture. We calculated the particles number density using the 4D-STEM dataset, allowing us to create virtual apertures to take into account the signal from all particles in the field of view.

Shearable particles make up ~93 % of N and give ~81 ± 53 MPa gain in strength; the remaining 7 % are considered as non-shearable, providing a contribution of ~318 ± 36 MPa to the yield strength. It is evident that this contribution to the strength is significantly over-estimated. One plausible explanation for the overestimation lies in the uncertain nature of particles in the deformed state after AA at 160 °C. Based on our observations, it has been determined that a vast majority of precipitates, ~90 %, exhibit partially disordered or defective structures. This structural characteristic can potentially facilitate dislocation cutting through the particles, even if their size exceeds a critical threshold. In addition, the threshold for the particle size for the transition from shearable to non-shearable was made for a very specific alloy, and for the material studied in this work it may be different. Therefore, we assume these larger particles also to be shearable, which gives ~112 ± 45 MPa. In total, this yields 193 ± 70 MPa contribution to the strength.

Solid solutions strengthening arises from variations in atom size between the Al matrix and solutes. This variation results in the creation of a long-range stress field that influences dislocation glide. The contribution from solid solution strengthening to the yield stress can be written according to Myhr et al. as [14].

$$\sigma_i = k_i C_i^{2/3}, \tag{6}$$

here σ_i is the strengthening contribution of solute i, k_i is a scaling factor for solute i ($k_{Mg} \approx 29$ and $k_{Si} \approx 66.3$ MPa (wt. %)$^{-2/3}$), and C_i is the concentration of solute i in wt. %. The EDX analysis may not be a reliable method to determine the remaining amount of Mg and Si in the Al-based solid solution; due to their low concentration, this leads to a high measurements inaccuracy. The most dependable approach instead would be to use Vegard's law. However, the available data for ternary alloys only provide lattice parameter *vs.* solute concentration relations for some specific Mg/Si ratios in Al–Mg–Si alloys. Furthermore, based on the data available the mutual influence of Si and Mg content is not a linear function of their total amount [60]. We estimated the residual concentration of solutes based on the volume fraction of secondary phase particles, and on the amount of substance needed for their formation. This procedure is described in more detail in the SI. With the determined residual Si and Mg solid solution concentration of 0.73 ± 0.01 and 0.2 ± 0.01 %, their contribution of the solid solution to the total strength of the alloy is 63 ± 30 MPa.

The calculated yield strength of the deformed 6101 Al alloy after AA at 160 °C according to Eq. (1) is 435 ± 77 MPa. The predicted value of σ_{total} turned out to be overestimated compared to the measured value (375 MPa). Several factors contribute to the discrepancy between the calculated and experimental values of the yield strength. Firstly, an inaccurate estimate of the contribution from solid solution strengthening is notable. This inaccuracy is linked to errors in determining the residual concentration of solutes, which does not take into account the

precipitates at grain boundaries. Additionally, another source of error here relates to the estimation of average particle composition performed using APT (data are not included in this study). Significant local magnification artifacts in the APT measurements lead to inaccurate determination of aluminum content in nano-size precipitates, and ultimately to quite high error in determination of solutes concentration. Secondly, it should be noted that the contribution to yield strength from precipitation hardening is directly proportional to the square of the particle size. As demonstrated, the secondary phase particles in the alloy exhibit a core-shell structure (Fig. 10d). In this context, the shell can be considered a transitional layer between the central part of the particle and the Al-based solid solution, possessing properties distinct from the core concerning resistance to dislocation glide. Consequently, including the particle shell in the calculation of dispersion strengthening can lead to a significant overestimation of the contribution of this mechanism. Thirdly, the modeling was conducted using microstructure data obtained at the middle of radius of the sample. However, the central part of the sample also influences the overall tensile strength. Therefore, the microstructure gradient across the sample from the center to the mid radius, introduces some inaccuracy in the strength modeling.

The summary of the contribution of microstructural features to strengthening in this model is presented in Fig. 16 for all three states. The structural characteristics for the deformed sample and after artificial aging at 130 °C are mentioned in Table S1.

4.5. EC modeling based on microstructural parameters

All strengthening mechanisms discussed above cause lattice distortions that affect the electrical resistivity of metals and alloys. The Matthiessen's rule [61] is used to take into account the influence of microstructural characteristics on the electrical resistivity. The total electrical resistivity ρ_{total} can be described as a sum of the contributions from each individual mechanism:

$$\rho_{total} = \rho_{Al} + \Lambda\rho_{dis} + S_{GB}\rho_{GB} + \frac{\rho_{prec}}{\sqrt{(L)}} + \sum C_i^{sol} \rho_i^{sol}, \tag{7}$$

where ρ_{Al} is the resistivity of the ideal Al lattice; ρ_{Al} was assumed to be 2.79 × 10^{-6} Ω·cm, measured for AA1350–O at room temperature (equivalent to 61.8 %IACS) [9]. The other terms in Eq. (2) stand for the contribution from dislocations, grain boundaries, solute atoms and precipitates. ρ_{dis} and ρ_{GB} were determined to be 2.7 × 10^{-25} Ω·m^3 and 2.6 × 10^{-16} Ω·m^2 in Ref. [62]; Λ is the dislocation density, which was obtained by X-ray diffraction data (Table 3), and S_{GB} is the fraction of the grain boundary area. In this study, a Kelvin tetrakaidecahedron model has been used as the best one to fill the space with full density [63]. Based on this model, for a material with an average grain size d, S_{GB} can be calculated as 3.3/d. With this, the contribution of dislocations and grain boundaries to the electrical resistivity are 9 × 10^{-9} Ω·cm and 2 × 10^{-8} Ω·cm. These values are several orders of magnitude lower than the resistivity of pure aluminum. Therefore, the contribution of these two mechanisms can be ignored.

The contribution from the precipitates ($\frac{\rho_{prec}}{\sqrt{(L)}}$) was calculated based on the method described in Ref. [62]. In this approach, ρ_{prec} was determined to be 12 Ω·nm$^{3/2}$ and L represents the inter-particle spacing in nanometers. which is calculated as $L = N^{-1/3}$ as described in the preceding section, yields values of 17 ± 1 nm for small precipitates and 41 nm for larger precipitates, in agreement well with (HR)TEM micrographs. Since the number of large particles is low, it is difficult to statistically estimate the error associated with the inter-particle spacing. Therefore, the precipitates' contribution to resistivity was quantified as 0.47 × 10^{-6} ± 1.1 × 10^{-9} Ω·cm.

The corresponding factors in Eq. (2) for the Mg and Si solutes were taken from Ref. [14]: $\rho_{sol}^{Mg} = 0.445 \times 10^{-6}$, and $\rho_{sol}^{Si} = 0.496 \times 10^{-6}$ Ω·cm/at. %. The addition to the total resistivity from the solute atoms
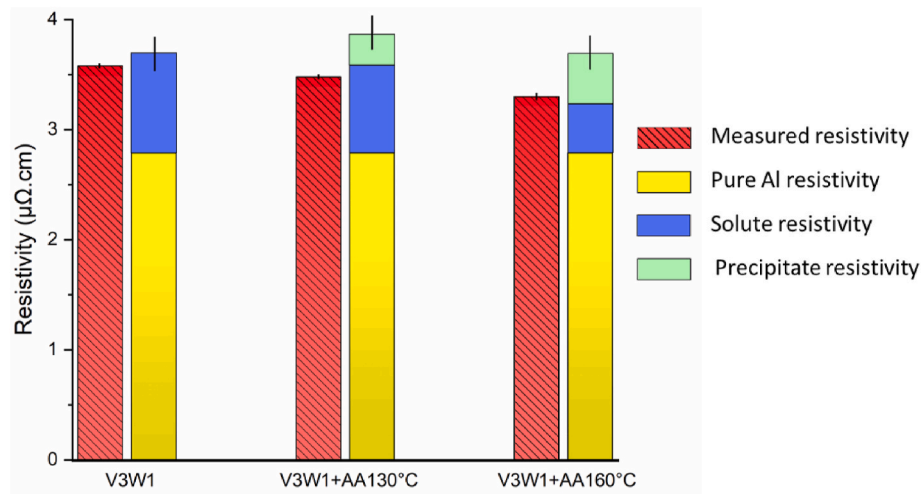
Fig. 17. Comparison of the measured and the modeled resistivity values based on the structural characteristics for the samples in as-deformed state and after AA at 130 and 160 °C. Different colors show the contributions from different mechanisms. (For interpretation of the references to color in this figure legend, the reader is referred to the Web version of this article.)

was estimated around $0.45 \times 10^{-6} \pm 0.3 \times 10^{-6}$ Ω·cm.

Thus, the total electrical resistivity was determined to be 3.71 μΩ·cm. The corresponding EC value can be calculated as EC (%$IACS$) = $172.4/\rho_{total}(\mu\Omega cm) = 46 \pm 3.7 \% IACS$ [64].

The source of discrepancy between measured and modeled values mentioned in strength modeling also affects resistivity modeling. Furthermore, for modeling the resistivity, we used the values measured for the mid-radius of the sample, whereas the experimental resistivity represents the average value for the entire sample. The comparison of the measured and calculated values of resistivity in three structural states is plotted in Fig. 17. The presence of impurities in the solid solution has a greater influence on the resistivity compared to the influence of precipitates.

5. Conclusions

Fine grained Al alloys were fabricated from a commercial Al 6101 alloy using HPTE. The microstructure, mechanical properties and electrical conductivity after processing and subsequent AA were comprehensively investigated. The following conclusions can be drawn:

- Samples processed by HPTE followed by AA at 160 °C for 10 h showed the best combination of yield strength (375 MPa), hardness (125 HV), uniform elongation to failure (~5 %), and EC (53 % IACS %), significantly improved compared to the standard T81 Al alloys used for electrical conductors with HV ~ 90 and EC ~ 54 %. Thus, a high strength – high conductivity state of the Al–Mg–Si alloy was successfully produced.
- During AA, the formation of nano-scale precipitates occurs with the particle size increasing with aging temperature. This precipitation process is accompanied by purification of the Al-based solid solution.
- The mechanism behind the formation of a high strength – high conductivity structural state involves the mutual action of nano-scaled secondary phase particles and purification of the solid solution. The processing conditions were optimized to adjust the size and particle density of the hardening phases and the degree of purification of the Al-based solid solution.
- The measured EC and yield strength values are in good agreement with the quantitative estimate of the respective values determined based on the contribution of different structural defects.

CRediT authorship contribution statement

Vahid Tavakkoli: Investigation, Writing – original draft. **Evgeniy Boltynjuk:** Data curation. **Torsten Scherer:** Writing – review & editing. **Andrey Mazilkin:** Conceptualization, Writing – review & editing. **Yulia Ivanisenko:** Methodology, Supervision, Writing – review & editing. **Tamas Ungar:** Data curation, Software. **Christian Kübel:** Resources, Supervision, Writing – review & editing.

Declaration of competing interest

The authors declare that they have no known competing financial interests or personal relationships that could have appeared to influence the work reported in this paper.

Data availability

Data will be made available on request.

Appendix A. Supplementary data

Supplementary data to this article can be found online at https://doi.org/10.1016/j.msea.2024.146556.

References

[1] H. Jin, The solid solution and grain boundary hardening due to Mg in an aluminum alloy system at room and Elevated temperatures, Metall. Mater. Trans. A 49 (12) (2018) 6122–6133, https://doi.org/10.1007/s11661-018-4949-9.

[2] G. Lin, Z. Zhang, H. Wang, K. Zhou, Y. Wei, Enhanced strength and electrical conductivity of Al–Mg–Si alloy by thermo-mechanical treatment, Mater. Sci. Eng. A 650 (2016) 210–217, https://doi.org/10.1016/j.msea.2015.10.050.

[3] Q. Zhao, Z. Qian, X. Cui, Y. Wu, X. Liu, Influences of Fe, Si and homogenization on electrical conductivity and mechanical properties of dilute Al–Mg–Si alloy, J. Alloys Compd. 666 (2016) 50–57, https://doi.org/10.1016/j.jallcom.2016.01.110.

[4] S. Karabay, Influence of AlB2 compound on elimination of incoherent precipitation in artificial aging of wires drawn from redraw rod extruded from billets cast of alloy AA-6101 by vertical direct chill casting, Mater. Des. 29 (7) (2008) 1364–1375, https://doi.org/10.1016/j.matdes.2007.06.004.

[5] E. Cervantes, M. Guerrero, J.A. Ramos, S.A. Montes, Influence of natural aging and cold deformation on the mechanical and electrical properties of 6201-T81 aluminum alloy wires, MRS Online Proc. Libr. 1275 (2010).

[6] F. Kiessling, P. Nefzger, J.F. Nolasco, U. Kaintzyk, Overhead Power Lines: Planning, Design, Construction, vol. 759, Springer, 2003.

[7] W. Yuan, Z. Liang, C. Zhang, L. Wei, Effects of La addition on the mechanical properties and thermal-resistant properties of Al–Mg–Si–Zr alloys based on AA 6201, Mater. Des. 34 (2012) 788–792, https://doi.org/10.1016/j.matdes.2011.07.003.

[8] J.P. Hou, et al., Origin of abnormal strength-electrical conductivity relation for an Al–Fe alloy wire, Materialia 7 (August) (2019), https://doi.org/10.1016/j.mtla.2019.100403.

[9] S.N. Khangholi, M. Javidani, A. Maltais, X.-G. Chen, Effects of natural aging and pre-aging on the strength and electrical conductivity in Al-Mg-Si AA6201 conductor alloys, Mater. Sci. Eng. A 820 (2021) 141538, https://doi.org/10.1016/j.msea.2021.141538.

[10] M. Furukawa, Z. Horita, M. Nemoto, T.G. Langdon, Review: processing of metals by equal-channel angular pressing, J. Mater. Sci. 36 (12) (2001) 2835–2843, https://doi.org/10.1023/A:1017932417043.

[11] Y. Saito, H. Utsunomiya, N. Tsuji, T. Sakai, Novel ultra-high straining process for bulk materials—development of the accumulative roll-bonding (ARB) process, Acta Mater. 47 (2) (1999) 579–583, https://doi.org/10.1016/S1359-6454(98)00365-6.

[12] A.P. Zhilyaev, T.G. Langdon, Using high-pressure torsion for metal processing: Fundamentals and applications, Prog. Mater. Sci. 53 (6) (2008) 893–979, https://doi.org/10.1016/j.pmatsci.2008.03.002.

[13] R.Z. Valiev, M.Y. Murashkin, I. Sabirov, A nanostructural design to produce high-strength Al alloys with enhanced electrical conductivity, Scripta Mater. 76 (2014) 13–16, https://doi.org/10.1016/j.scriptamat.2013.12.002.

[14] X. Sauvage, E.V. Bobruk, M.Y. Murashkin, Y. Nasedkina, N.A. Enikeev, R.Z. Valiev, Optimization of electrical conductivity and strength combination by structure design at the nanoscale in Al-Mg-Si alloys, Acta Mater. 98 (2015) 355–366, https://doi.org/10.1016/j.actamat.2015.07.039.

[15] Y. Ivanisenko, et al., High Pressure Torsion Extrusion as a new severe plastic deformation process, Mater. Sci. Eng. A 664 (2016) 247–256, https://doi.org/10.1016/j.msea.2016.04.008.

[16] B. Omranpour, et al., Evolution of microstructure and hardness in aluminum processed by high pressure torsion extrusion, Mater. Sci. Eng. A 762 (2019) 138074.

[17] B. Omranpour, et al., Tailoring the microstructure and tribological properties in commercially pure aluminium processed by High Pressure Torsion Extrusion, Proc. Est. Acad. Sci. 70 (4) (2021) 540–548.

[18] D. Nugmanov, A. Mazilkin, H. Hahn, Y. Ivanisenko, Structure and tensile strength of pure Cu after high pressure torsion extrusion, Metals 9 (10) (2019), https://doi.org/10.3390/met9101081.

[19] A. Fata, G. Faraji, M. Mosavi Mashadi, V. Tavakkoli, Hot deformation behavior of Mg-Zn-Al alloy tube processed by severe plastic deformation, Arch. Metall. Mater. 62 (1) (2017), https://doi.org/10.1515/amm-2017-0022.

[20] F.J. Humphreys, Characterisation of fine-scale microstructures by electron backscatter diffraction (EBSD), Scripta Mater. 51 (8) (2004) 771–776, https://doi.org/10.1016/j.scriptamat.2004.05.016.

[21] G. Ribárik, B. Jóni, T. Ungár, The convolutional multiple whole profile (CMWP) fitting method, a global optimization procedure for microstructure determination, Crystals 10 (7) (2020), https://doi.org/10.3390/cryst10070623.

[22] M. Wojdyr, Fityk: a general-purpose peak fitting program, J. Appl. Crystallogr. 43 (5) (Oct. 2010) 1126–1128, https://doi.org/10.1107/S0021889810030499 [Online]. Available:.

[23] B. S. EN, 50183:'Conductors for Overhead Lines–Aluminiummagnesium-Silicon Alloy Wires, Br. Stand., 2000.

[24] R. Kulagin, Y. Beygelzimer, Y. Estrin, Y. Ivanisenko, B. Baretzky, H. Hahn, A mathematical model of deformation under high pressure torsion extrusion, Metals 9 (3) (2019) 1–11, https://doi.org/10.3390/met9030306.

[25] C.D. Marioara, et al., HAADF-STEM study of β′-type precipitates in an over-aged Al–Mg–Si–Ag alloy, Philos. Mag. A 92 (9) (2012) 1149–1158.

[26] H.J. Roven, M. Liu, J.C. Werenskiold, Dynamic precipitation during severe plastic deformation of an Al–Mg–Si aluminium alloy, Mater. Sci. Eng. A 483 (484) (2008) 54–58, https://doi.org/10.1016/j.msea.2006.09.142.

[27] M. Liu, et al., DSC analyses of static and dynamic precipitation of an Al–Mg–Si–Cu aluminum alloy, Prog. Nat. Sci. Mater. Int. 88 (May 2015), https://doi.org/10.1016/j.pnsc.2015.02.004.

[28] Z. Horita, T. Fujinami, M. Nemoto, T.G. Langdon, Equal-channel angular pressing of commercial aluminum alloys: grain refinement, thermal stability and tensile properties, Metall. Mater. Trans. A 31 (3) (2000) 691–701, https://doi.org/10.1007/s11661-000-0011-8.

[29] E. Christiansen, C.D. Marioara, B. Holmedal, O.S. Hopperstad, R. Holmestad, "Nano-scale characterisation of sheared β" precipitates in a deformed Al-Mg-Si alloy,", Sci. Rep. 9 (1) (2019) 17446 https://doi.org/10.1038/s41598-019-53772-4.

[30] O. Engler, C.D. Marioara, Y. Aruga, M. Kozuka, O.R. Myhr, Effect of natural ageing or pre-ageing on the evolution of precipitate structure and strength during age hardening of Al–Mg–Si alloy AA 6016, Mater. Sci. Eng. A 759 (2019) 520–529, https://doi.org/10.1016/j.msea.2019.05.073.

[31] A.P. Sekhar, A. Samaddar, A.B. Mandal, D. Das, Influence of ageing on the intergranular corrosion of an Al–Mg–Si alloy, Met. Mater. Int. 27 (12) (2021) 5059–5073, https://doi.org/10.1007/s12540-020-00843-1.

[32] W. Yang, S. Ji, Z. Li, M. Wang, Grain boundary precipitation induced by grain crystallographic misorientations in an extruded Al–Mg–Si–Cu alloy, J. Alloys Compd. 624 (2015) 27–30, https://doi.org/10.1016/j.jallcom.2014.10.206.

[33] G. Nurislamova, X. Sauvage, M. Murashkin, R. Islamgaliev, R. Valiev, Nanostructure and related mechanical properties of an Al–Mg–Si alloy processed by severe plastic deformation, Phil. Mag. Lett. 88 (6) (2008) 459–466, https://doi.org/10.1080/09500830802186938.

[34] E. Christiansen, C.D. Marioara, K. Marthinsen, O.S. Hopperstad, R. Holmestad, Lattice rotations in precipitate free zones in an Al-Mg-Si alloy, Mater. Char. 144 (2018) 522–531, https://doi.org/10.1016/j.matchar.2018.08.002.

[35] B.D. Cullity, Elements of X-Ray Diffraction, Addison-Wesley Publishing, 1956.

[36] W. Chrominski, M. Lewandowska, Influence of dislocation structures on precipitation phenomena in rolled Al–Mg–Si alloy, Mater. Sci. Eng. A 793 (2020) 139903, https://doi.org/10.1016/j.msea.2020.139903.

[37] J. Weertman, Dislocation Based Fracture Mechanics, World Scientific, 1996.

[38] M. Fourmeau, C.D. Marioara, T. Børvik, A. Benallal, O.S. Hopperstad, A study of the influence of precipitate-free zones on the strain localization and failure of the aluminium alloy AA7075-T651, Philos. Mag. A 95 (28–30) (2015) 3278–3304.

[39] S. Peng, Y. Wei, H. Gao, Nanoscale precipitates as sustainable dislocation sources for enhanced ductility and high strength, Proc. Natl. Acad. Sci. USA 117 (10) (2020) 5204–5209.

[40] Y. Zhang, et al., Dynamic precipitation, segregation and strengthening of an Al-Zn-Mg-Cu alloy (AA7075) processed by high-pressure torsion, Acta Mater. 162 (2019) 19–32, https://doi.org/10.1016/j.actamat.2018.09.060.

[41] S.J. Andersen, H.W. Zandbergen, J. Jansen, C. TrÆholt, U. Tundal, O. Reiso, The crystal structure of the β″ phase in Al–Mg–Si alloys, Acta Mater. 46 (9) (1998) 3283–3298, https://doi.org/10.1016/S1359-6454(97)00493-X.

[42] K. Teichmann, et al., HRTEM study of the effect of deformation on the early precipitation behaviour in an AA6060 Al-Mg-Si alloy, Philos. Mag. A 91 (28) (2011) 3744–3754, https://doi.org/10.1080/14786435.2011.593577.

[43] R.S. Yassar, D.P. Field, H. Weiland, The effect of predeformation on the β″ and β′ precipitates and the role of Q′ phase in an Al–Mg–Si alloy; AA6022, Scripta Mater. 53 (3) (2005) 299–303, https://doi.org/10.1016/j.scriptamat.2005.04.013.

[44] J.Y. Yao, D.A. Graham, B. Rinderer, M.J. Couper, A TEM study of precipitation in Al–Mg–Si alloys, Micron 32 (8) (2001) 865–870, https://doi.org/10.1016/S0968-4328(00)00095-0.

[45] T. Saito, et al., Atomic structures of precipitates in Al–Mg–Si alloys with small additions of other elements, Adv. Eng. Mater. 20 (7) (2018) 1800125.

[46] P.H. Ninive, et al., Detailed atomistic insight into the β″ phase in Al–Mg–Si alloys, Acta Mater. 69 (2014) 126–134, https://doi.org/10.1016/j.actamat.2014.01.052.

[47] A.J. Ardell, On the coarsening of grain boundary precipitates, Acta Metall. 20 (4) (1972) 601–609, https://doi.org/10.1016/0001-6160(72)90015-6.

[48] C.-S. Tsao, C.-Y. Chen, U.-S. Jeng, T.-Y. Kuo, Precipitation kinetics and transformation of metastable phases in Al–Mg–Si alloys, Acta Mater. 54 (17) (2006) 4621–4631, https://doi.org/10.1016/j.actamat.2006.06.005.

[49] T. Ogura, A. Hirose, T. Sato, Effect of PFZ and grain boundary precipitate on mechanical properties and fracture morphologies in Al–Zn-Mg (Ag) Alloys, in: Materials Science Forum, vol. 638, 2010, pp. 297–302.

[50] B.H. Frodal, E. Christiansen, O.R. Myhr, O.S. Hopperstad, The role of quench rate on the plastic flow and fracture of three aluminium alloys with different grain structure and texture, Int. J. Eng. Sci. 150 (2020) 103257, https://doi.org/10.1016/j.ijengsci.2020.103257.

[51] Y. Han, et al., Effect of Mg/Si ratio on the microstructure and hardness–conductivity relationship of ultrafine-grained Al–Mg–Si alloys, J. Mater. Sci. 52 (8) (2017) 4445–4459.

[52] M.H. Mulazimoglu, R.A.L. Drew, J.E. Gruzelski, Electrical conductivity of aluminium-rich Al-Si-Mg alloys, J. Mater. Sci. Lett. 8 (3) (1989) 297–300, https://doi.org/10.1007/BF00725503.

[53] M.Y. Murashkin, I. Sabirov, V.U. Kazykhanov, E. V Bobruk, A.A. Dubravina, R.Z. Valiev, Enhanced mechanical properties and electrical conductivity in ultrafine-grained Al alloy processed via ECAP-PC, J. Mater. Sci. 48 (2013) 4501–4509.

[54] M. Murashkin, et al., Enhanced mechanical properties and electrical conductivity in ultrafine-grained Al 6101 alloy processed via ECAP-conform, Metals 5 (4) (2015) 2148–2164, https://doi.org/10.3390/met5042148.

[55] J.G. Kaufman, Understanding the aluminum temper designation system, Introd. to Alum. Alloy. Tempers (2000) 39–76 [Online]. Available: https://www.scopus.com/inward/record.uri?eid=2-s2.0-85030103049&partnerID=40&md5=f5c e1590397d78d6cfd9732775d28011.

[56] K. Ma, et al., Mechanical behavior and strengthening mechanisms in ultrafine grain precipitation-strengthened aluminum alloy, Acta Mater. 62 (2014) 141–155, https://doi.org/10.1016/j.actamat.2013.09.042.

[57] J.P. Hou, et al., Origin of abnormal strength-electrical conductivity relation for an Al–Fe alloy wire, Materialia 7 (2019) 100403, https://doi.org/10.1016/j.mtla.2019.100403.

[58] N. Hansen, Hall–Petch relation and boundary strengthening, Scripta Mater. 51 (8) (2004) 801–806, https://doi.org/10.1016/j.scriptamat.2004.06.002.

[59] S. Thangaraju, M. Heilmaier, B.S. Murty, S.S. Vadlamani, On the estimation of true Hall–Petch constants and their role on the superposition law exponent in Al alloys, Adv. Eng. Mater. 14 (10) (2012) 892–897.

[60] W.B. $$Qpearso, William B. Pearson, William B. Pearson, A Handbook of Lattice Spacings and Structures of Metals and Alloys), vol. 2, 1967.

[61] S. Nikzad Khangholi, M. Javidani, A. Maltais, X.-G. Chen, Optimization of mechanical properties and electrical conductivity in Al–Mg–Si 6201 alloys with

different Mg/Si ratios, J. Mater. Res. 35 (20) (2020) 2765–2776, https://doi.org/10.1557/jmr.2020.249.

[62] B. Raeisinia, W.J. Poole, D.J. Lloyd, Examination of precipitation in the aluminum alloy AA6111 using electrical resistivity measurements, Mater. Sci. Eng. A 420 (1) (2006) 245–249, https://doi.org/10.1016/j.msea.2006.01.042.

[63] W. Thomson, LXIII. On the division of space with minimum partitional area, Mag. J. Sci. 24 (151) (Dec. 1887) 503–514, https://doi.org/10.1080/14786448708628135. London, Edinburgh, Dublin Philos.

[64] W. Wen, Y. Zhao, J.G. Morris, The effect of Mg precipitation on the mechanical properties of 5xxx aluminum alloys, Mater. Sci. Eng. A 392 (1) (2005) 136–144, https://doi.org/10.1016/j.msea.2004.09.059.